Stony Brook University

Lattice Boltzmann Simulation of Immiscible Two-Phase Flow in Three Dimensional Porous Media

A Dissertation Presented
by

Hagos Mehreteab Kifle

to
The Graduate School in Partial Fulfillment of the Requirements for the Degree of
Doctor of Philosophy

in

Applied Mathematics and Statistics
Stony Brook University

August 2008

Stony Brook University

The Graduate School

Hagos Mehreteab Kifle

We, the dissertation committee for the above candidate for the
Doctor of Philosophy degree, hereby recommend
acceptance of this dissertation.

W. Brent Lindquist
Professor of Applied Mathematics
Dissertation Advisor

Joseph S. B. Mitchell
Professor of Applied Mathematics
Chairman of Defense

Xiaolin Li
Professor of Applied Mathematics
Committee Member

Arie E. Kaufman
Professor of Computer Science, Stony Brook University
Outside Member

This Dissertation is accepted by the Graduate School

Lawrence Martin
Dean of the Gradate School

Abstract of the Dissertation

Lattice Boltzmann Simulation of Immiscible Two-Phase Flow in Three Dimensional Porous Media

by

Hagos Mehreteab Kifle

Doctor of Philosophy

in

Applied Mathematics and Statistics

Stony Brook University

2008

Multiphase flow in porous media at the pore scale is of major interest in oil recovery, degradation of building materials, the spread of hazardous wastes in the ground, contaminant remediation in aquifers, and the containment of nuclear wastes. The challenges in simulating two-phase flow in a porous media include its geometrical complexity and the vastness of the physical and geochemical parameters to be incorporated in the model.

Unlike traditional computational schemes, the lattice Boltzmann model uses particle distribution functions to evolve macroscopic quantities such as density and velocity. For two phase flow, the model must incorporate fluid particles that collide with particles of their own type, other fluid particles and an obstacle (wall boundaries) under an applied external body force. The no-slip bounce back boundary condition is used for particle-wall collisions and periodic boundary conditions are used at the inlet-outlet ends of the domain. The Shan-Chen potential is employed to model the interaction (collisions) between the two phases.

Phase relative permeabilities as a function of resident fluid saturation are computed for the bulk media using Darcy's law. The effects of different viscosities, pressure gradient and fluid-fluid interaction constants in the model are studied extensively.

To my home university, University of Asmara

Table of Contents

List of Figures

List of Tables

Acknowledgements

I would like to thank my advisor Professor W. Brent Lindquist for his continuous guidance and deep knowledge. My profound thanks to my late mother Aregash, my father Mehreteab, my sisters and brothers, and my cousin Elsa for their encouragement, love and patience. Furthermore, I would like to thank Dr. Moquanint Moges for his continuous encouragement, Henok Tesfai for his friendship, and Xi Cheng for sharing information and discussion of technical issues.

Chapter 1

Introduction

Simulating multiphase fluid flow in porous media has been an important field of study due to its varied applications in physical sciences, life sciences, and engineering. Major applications are in the study of oil recovery, degradation of building materials, the spread of hazardous wastes in the ground, contaminant remediation in aquifers, chemical processing, combustion mixing and reaction, and the containment of nuclear wastes.

In today's oil market, economic production of oil and gas resources requires carefully engineered recovery projects of increasing technical complexity and sophistication. Hydrocarbons do not reside in easily accessible pools awaiting discovery. Usually they are found at enormous depths within the pore networks of sedimentary deposits. In the complicated structure of pore network pathways there is significant impedance to the flow of oil towards the production well. Furthermore, since water resides in some of the pores, oil and water are recovered simultaneously at the well-head. Even though large quantities of oil are known to reside in a reservoir, often only a relatively small fraction of it can be recovered with conventional pumping technology. The most common method of enhancing oil recovery is the injection of water toward the production wells [7] as illustrated in Fig. 1.1.

Recovery of subsurface fluids requires understanding the ways fluid(s) flow within porous and fractured rocks and soil. This is particularly complicated in the presence of multiple fluids. Experiments, combined with theoretical and computational modeling, have tracked the flow of two phases in fractured and porous media and show how both phases move competitively. Each phase separately responds to capillary pressure, gravity and viscous forces. The relative mobility of any phase is a function of the surface tension of phase boundaries, and one phase may act as a barrier to the flow of the other. As a result, flow paths for a given fluid phase are significantly longer than under single-phase conditions and transport is very sensitive to differences in phase structure, even at relatively similar values of phase saturation and relative permeability of the two phases [52].

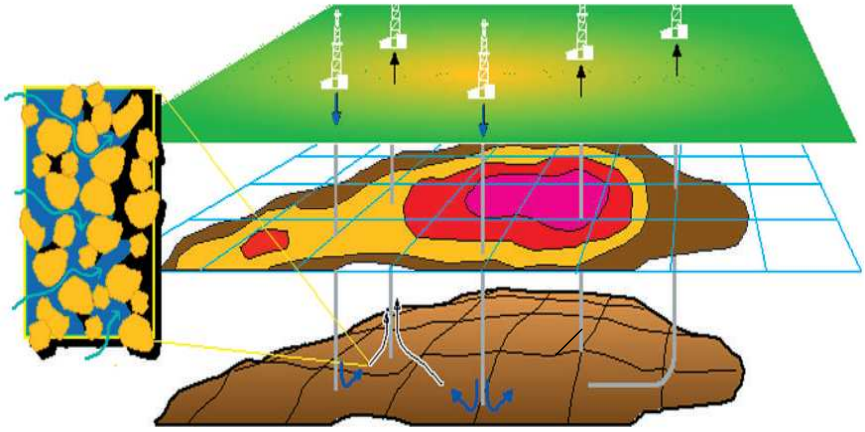

Figure 1.1: An illustration of a modern oil-recovery project. Water is depicted invading the pore network of a porous rock filled with oil (left). A simplified grid discretization at a field scale recovery process (right) (after [7]).

1.1 The Study of Fluid Motion in Porous Media

The study of fluid motion covers a wide field, from the problems of creeping flow, controlled by viscous forces, to those of very high speed Reynolds number, controlled by inertia and compressibility forces. Scale analysis (the simplification of equations with many terms by determining the approximate magnitude of individual terms and ignoring negligibly small terms) and conservation laws have been the traditional guiding principles for approximating the equations of fluid motion. The governing equations for fluid motion in porous media are the mass continuity equation

$$\frac{\partial \rho}{\partial t} + \nabla \cdot (\rho \vec{u}) = 0, \tag{1.1}$$

and the Navier-Stokes equation (conservation of momentum)

$$\frac{\partial \vec{u}}{\partial t} + \vec{u} \cdot \nabla \vec{u} = -\frac{\nabla P}{\rho} + \nu \nabla^2 \vec{u} \tag{1.2}$$

for a fluid with density ρ, velocity $\vec{u}$, pressure P and kinetic viscosity ν. Equation (1.2) is a second order partial differential equation which has no known analytic solution, even for single phase flow, except in special cases. Analytic methods address the existence of solutions to flow problems under different conditions but do not provide closed form solutions. Numerical methods are used to find virtually all solutions.

1.2 Numerical Methods

The difficulty of carrying out laboratory and field experiments, measured in terms of expense, make numerical methods attractive tools in understanding fluid motion.

Challenges arise from the complexity of the geometry of the domain and number of phases under consideration. Numerical methods employing finite difference, finite volume and finite element techniques have been used extensively in studying fluid flow at the macroscopic scale level.

One scheme that can handle the complex geometry encountered at the pore scale is the *Lattice Boltzmann Method*. It has the property that its solutions approach those of the Navier-Stokes equations for slow-flow (low mach number) problems. The application of this method is the main topic of this dissertation.

1.3 Modeling Fluid Flow

The dynamics of fluid flows, which are generated at the microscopic level, could in principle be modeled with direct simulation at the molecular scale. In practice it is infeasible to solve macroscopic systems with such an approach due to the scarcity of computing resources and time required for molecular-scale simulation on macroscopic time scales. The challenge in modeling increases as we proceed from single to multi-phase flow. Oil reservoirs are complex geological formations. To simulate them, it is necessary to take solid, liquid, and gas phases into account, as well as any chemical reactions occurring among and between the phases. "This is the main challenge for porous media modeling, to handle highly nonlinear and hysteretic coupled flows with multiscale, multiphase, multicomponent, and multiphysics features" [46].

1.4 Input Data Acquisition

A description of the geometry of the porous material in which the fluid is flowing is crucial in determining transport properties such porosity, tortuosity and permeability. Porous media data sets vary from model media (eg. sphere packs) to samples taken from geologic deposits. The most widely used model consists of artificial sphere packs. Artificial sphere packs are considerably different from rocks which are drilled from oil wells. Use of X-ray computed microtomographic imaging of geologic samples helps to avoid oversimplified models, resulting in improved data sets for understanding the transport properties of geologic media.

A powerful image generating technique, X-ray computed microtomography generates 3D images of porous rocks. It provides the opportunity to directly measure the complex morphology of pore space of the sedimentary rock at a resolution down to few microns. As a result, synthetic images are replaced by X-ray computed microtomographic (XCMT) images. XCMT discretizations of Fontainebleau sandstone of different porosities and sizes are used as input data to the two-phase lattice Boltzmann simulations in this thesis.

1.5 Objectives

The main objectives of this work are:

1. Understanding and quantifying the transport properties of two flowing fluid phases at the pore scale. We consider the effect on the residual resident phase saturation of:

   a) the strength of the pressure gradient, used as a driving force for the fluid flow;

   b) the variation in the relaxation time parameters (which model fluid viscosity) in the model;

   c) density differences of the invading and resident fluid phases.

2. Understanding and predicting the relative permeabilities of the two phases flowing through three dimensional Fontainebleau sandstone.

3. Understanding the interfacial properties (moving boundaries) of the fluid-fluid interaction. Four different values of the fluid-fluid interaction constant, G, are considered to study the interfacial interaction between the two phases.

The dissertation is organized as follows. In Chapter 2, we describe the Boltzmann transport equation and its relationship with the Navier-Stokes equation. Chapter 3 contains the details of the lattice Boltzmann model and the discretization of the Boltzmann equation. We describe the lattice Boltzmann model for two-phase flow in porous media in Chapter 4. Chapter 5 contains Fontainebleau sandstone analysis and simulation results. Conclusions are presented in Chapter 6.

Chapter 2

The Boltzmann Transport Equation

In this chapter the ideas underlying the Boltzmann equation of a fluid system in the context of classical statistical mechanics are reviewed. The Boltzmann equation, on which kinetic theory is highly dependent, was established by Ludwig Boltzmann in 1872. Here, the Boltzmann equation is reviewed and the macroscopic quantities of mass, momentum and energy are defined in terms of the distribution function of the fluid. It is shown that the Boltzmann description of the fluid satisfies the fluid conservation equations. The form of the collision operator for an ideal fluid, in which only binary collisions are considered, is reviewed.

2.1 The Classical Boltzmann Equation

Consider the motion of N mutually interacting molecules in a box of volume V at temperature T. Their microscopic dynamics is governed by the Newton equations

$$\frac{d\vec{x_i}}{dt} = \frac{\vec{p_i}}{m}, \tag{2.1}$$

$$\frac{d\vec{p_i}}{dt} = \vec{F_i}, \quad i = 1, \ldots, N, \tag{2.2}$$

where $\vec{x_i}$ is the position of the i-th molecule, $\vec{p_i} \equiv m\vec{v_i}$ is its linear momentum and $\vec{F_i}$ the force experienced by the molecule as a result of intermolecular interactions. With appropriate initial and boundary conditions, equations (2.1) and (2.2) form a system of $6N$ functions of time $[\vec{x_i}(t), \vec{p_i}(t)], i = 1, \ldots, N$ which can be solved in principle. Since N is a large number, it is not feasible to seek a direct solution for such equations. An approach which considers the collective behavior of the molecules from a statistical point of view simplifies the computational burden of the N-particle system.

Let $f(\vec{x}, \vec{p}, t)$ be the probability of finding a molecule at position $\vec{x}$ at time t with momentum $\vec{p}$. The quantity $\delta n(\vec{x}, \vec{p}, t) \equiv f(\vec{x}, \vec{p}, t)\delta\vec{x}\delta\vec{p}$ is the probable number of molecules in the position $\vec{x} \to \vec{x} + \delta\vec{x}$ having momentum $\vec{p} \to \vec{p} + \delta\vec{p}$. The distribution function $f(\vec{x}, \vec{p}, t)$ is the fundamental variable of the kinetic theory; the Boltzmann equation describes the evolution of f in terms of molecular interactions.

The kinetic equation for the distribution function, when all particles are of the same type, is

$$\partial_t f(\vec{x},\vec{v},t) + \frac{\vec{p}}{m}\cdot\nabla_{\vec{x}} f(\vec{x},\vec{p},t) + \vec{F}\cdot\nabla_{\vec{p}} f(\vec{x},\vec{p},t) = \Omega(f), \tag{2.3}$$

where the left hand side represents the streaming motion of the molecules along trajectories associated with the force field $\vec{F}$, which is similar to the Newtonian single particle dynamics, and $\Omega(f)$ represents the effect of intermolecular collisions moving molecules in and out the trajectory [64].

The intermolecular interactions can be described mainly in terms of localized binary collisions (Boltzmann theory assumption). The collision term splits into gain, G, and loss, L, components:

$$\Omega(f) \equiv G - L = \int d(\Omega) \int (f_{1'2'} - f_{12})\, |\vec{v}_1 - \vec{v}_2|\, \sigma(\Omega)\, d\vec{p}_2, \tag{2.4}$$

where f_{12} is the probability of finding, at time t, molecule 1 at $\vec{x}_1$ with velocity $\vec{v}_1$ and molecule 2 at $\vec{x}_2$ with velocity $\vec{v}_2$.

$\sigma(\Omega)$ is the differential scattering cross section which describes the probability density for any given change of velocities $\{\vec{v}_1,\vec{v}_2\} \to \{\vec{v}_1',\vec{v}_2'\}$. The subscripts 1, 2 and $1'$, $2'$ are states corresponding to direct $(\vec{v}_1,\vec{v}_2 \to \vec{v}_1',\vec{v}_2')$ and inverse $(\vec{v}_1',\vec{v}_2' \to \vec{v}_1,\vec{v}_2)$ collisions taking molecules out of/into the volume element $d\vec{v}_1 d\vec{v}_2$, respectively (see Fig. 2.1).

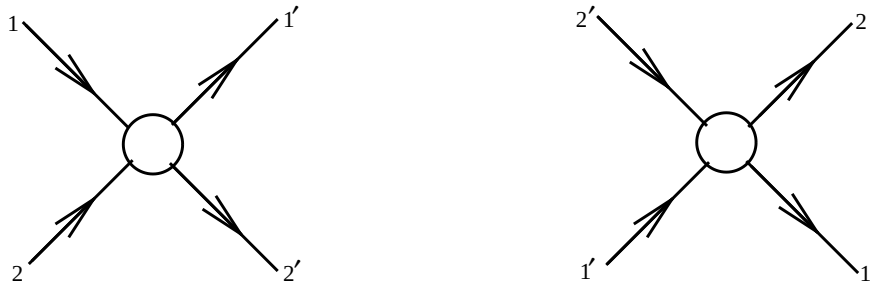

Figure 2.1: Direct (left) and inverse (right) intermolecular collision diagrams.

Using the Boltzmann *closure assumption*, $f_{12} = f_1 f_2$ [66], the Boltzmann equation (2.3) takes the form

$$\frac{\partial f}{\partial t} + \vec{v}\cdot\nabla_{\vec{x}} f + \vec{F}\cdot\frac{\partial f}{\partial \vec{p}} = \int d\Omega \int (f_{1'} f_{2'} - f_1 f_2)\, |\vec{v}_1 - \vec{v}_2|\, \sigma(\Omega)\, d\vec{p}_2, \tag{2.5}$$

where $f_1 = f(\vec{x},\vec{v}_1,t)$ and $f_{1'} = f(\vec{x},\vec{v}_1',t)$. Given an initial particle density function $f(\vec{x},\vec{v},0)$, the solution function $f(\vec{x},\vec{v},t)$ describes how the density function changes over time.

The fluid density ρ, velocity $\vec{u}$ and internal energy e can be obtained from the distribution function f [9] as follows:

$$\int m f(\vec{x},\vec{v},t)\,d\vec{v} = \rho(\vec{x},t); \tag{2.6}$$

$$\int m\vec{v} f(\vec{x},\vec{v},t)\,d\vec{v} = \rho(\vec{x},t)\vec{u}(\vec{x},t); \tag{2.7}$$

$$\frac{1}{2}\int m\vec{u}_0 f(\vec{x},\vec{v},t)\,d\vec{v} = \rho(\vec{x},t)e(\vec{x},t), \tag{2.8}$$

where m is the molecular mass and $\vec{u}_0$ is the *peculiar* velocity $\vec{u}_0 \equiv \vec{v} - \vec{u}$, i.e. the particle velocity relative to the average (or bulk) fluid flow velocity. The internal energy related to f can be shown to be [64]

$$e = \frac{3}{2m}RT,$$

where T is the temperature and R is the Boltzmann gas constant.

2.2 Collision Operator

To facilitate the numerical solution of the Boltzmann equation, the complicated nonlinear collision operator Ω of equation (2.4) is replaced by a simplified expression. There are at least two different general approaches that are currently in use to compute the collision operator. These are the:

1. Eggels-Somers model described by Somers [62] and Eggels and Somers [20], and used by Eggles [21] and Derksen and Van den Akker [17] to simulate single phase flow;

2. Bhatnagar-Gross-Krook (BGK) model which is widely used and is our choice in this work because it is easier to program than the former. It is based on a simplified kinetic equation for dilute gases [4]. See Qian [68], Chen et al. [10], and Qian et al. [53] for detailed explanation of the BGK model in the lattice Boltzmann method.

The simplified expression given by the BGK model for the collision operator [4] is

$$\Omega_{BGK}(f) = -\frac{f - f^e}{\tau}, \tag{2.9}$$

where f^e is the equilibrium particle distribution function, which depends on the local density, ρ, and the velocity, $\vec{v}$ and τ is a dimensionless relaxation time that depends on the kinematic viscosity, ν. τ is related to ν by the following equation,

$$\nu = \frac{1}{3}(\tau - \frac{1}{2}), \tag{2.10}$$

where $\tau > \frac{1}{2}$.

2.3 A Review of the Chapman-Enskog Expansion

Chapman and Enskog developed a multiscale analysis procedure [9] for the approximate solution of Boltzmann's equation. For certain simple models such as hard spheres their method produces predictions for $f(\vec{x}, \vec{v}, t)$ (or its moments) which can be tested in computer simulations [6]. The Chapman-Enskog procedure expands the particle distribution function $f(\vec{x}, \vec{v}, t)$ in terms of the independent space and time $(\vec{x}, t)$ variables in order to recover the Navier-Stokes equation.

The expansion uses a parameter, known as the *Knudsen number*, which is the ratio of the molecular mean free (particle) path λ to the macroscopic (continuum) characteristic length l,

$$K_n \equiv \epsilon = \frac{\lambda}{l}. \tag{2.11}$$

ϵ is introduced into the Boltzmann equation (2.5) in the following way,

$$t = \epsilon^{-1} t_1 + \epsilon^{-2} t_2, \tag{2.12}$$

$$\vec{x} = \epsilon^{-1} \vec{x}_1, \tag{2.13}$$

where t_1 and t_2 are fast and slow time-scales corresponding to convective and diffusive processes. The corresponding differential operator representations for equations (2.12) and (2.13) are

$$\frac{\partial}{\partial t} = \epsilon \frac{\partial}{\partial t_1} + \epsilon^2 \frac{\partial}{\partial t_2}, \tag{2.14}$$

$$\frac{\partial}{\partial x_a} = \epsilon \frac{\partial}{\partial x_{1a}}, \qquad a = 1, 2, 3. \tag{2.15}$$

A small Knudsen number, ϵ, is necessary for the convergence of expansion terms. Expansion moments of f are obtained by Taylor series expansion about $f^e (\equiv f^{(0)})$,

$$f = \sum_{n=0}^{\infty} \epsilon^n f^{(n)} = f^e + \epsilon f^{(1)} + \epsilon^2 f^{(2)} + \cdots . \tag{2.16}$$

Similarly expanding equation (2.5) up to second order in ϵ yields

$$\epsilon \frac{\partial f}{\partial t_1} + \epsilon^2 \frac{\partial f}{\partial t_2} + \epsilon v_a \frac{\partial f}{\partial x_{1a}} + \frac{1}{2} \epsilon^2 v_a v_b \frac{\partial^2 f}{\partial x_{1a} \partial x_{1b}} = \Omega(f^e) + \epsilon \frac{\partial \Omega(f^{(1)})}{\partial f}, \quad a, b = 1, 2, 3. \tag{2.17}$$

The value of the collision operator Ω at the equilibrium distribution function f^e is zero by (2.9). The expansions, to second order, (details are given in [27]) of the mass and momentum equations are

$$\epsilon \hat{M}_1 + \epsilon^2 \hat{M}_2 = 0, \tag{2.18}$$

$$\epsilon \hat{J}_1 + \epsilon^2 \hat{J}_2 = 0, \tag{2.19}$$

where $\hat{M}_i$, $\hat{J}_i$, $i = 1, 2$, are the i-th order differential form for mass and momentum respectively. At order ϵ, one obtains $\hat{M}_1 = 0$ and $\hat{J}_1 = 0$ (mass and momentum conservation requirement), which can be written as

$$\frac{\partial \rho}{\partial t_1} + \frac{\partial (\rho u_a)}{\partial x_{1a}} = 0, \tag{2.20}$$

$$\frac{\partial (\rho u_a)}{\partial t_1} + \frac{\partial (\rho u_a u_b)}{\partial x_{1b}} = -c_s^2 \frac{\partial \rho}{\partial x_{1a}}. \tag{2.21}$$

Equation (2.21) can be rewritten as

$$\frac{\partial (\rho u_a)}{\partial t_1} + \frac{\partial (\rho u_a u_b)}{\partial x_{1b}} = -\frac{\partial}{\partial x_{1b}} \left(\frac{\rho(1-d_0)}{2} c^2 \delta_{ab} \right). \tag{2.22}$$

This is an Euler equation for inviscid flow without dissipation.

2.4 The Navier-Stokes Equations

The Navier-Stokes equations can be derived using the second order terms from (2.18) and (2.19), and are more complicated due to the involvement of equilibrium and non-equilibrium terms and mixed space-time derivatives. The final result is relatively simple [43] and can be stated as

$$\frac{\partial \rho}{\partial t_1} + \frac{\partial (\rho u_a)}{\partial x_{1a}} = 0, \tag{2.23}$$

$$\frac{\partial (\rho u_a)}{\partial t_1} + \frac{\partial (\rho u_a u_b)}{\partial x_{1b}} = -\frac{\partial}{\partial x_{1b}} \left(\frac{\rho(1-d_0)}{2} c^2 \delta_{ab} \right) + \nu \nabla^2 \rho u_a + \frac{\partial}{\partial x_{1a}} (\mu \nabla \cdot \rho \vec{u}), \tag{2.24}$$

where ν is the kinematic viscosity and μ is the dynamic viscosity.

In the next chapters, details of the Boltzmann equation and lattice Boltzmann model are addressed.

Chapter 3

The Lattice Boltzmann Model

In the last two decades, the lattice Boltzmann method (LBM) has emerged as a potentially powerful numerical scheme for simulating fluid flow. Initially developed to overcome certain deficiencies of lattice gas cellular automaton (statistical noise [55] and lack of Galilean invariance [70]), the LBM has undergone continuous development. The lattice Boltzmann equation can be derived as an approximate solution to the Boltzmann equation (2.5). Unlike traditional numerical methods which solve partial differential equations directly at the macroscopic level, the lattice Boltzmann equation solves the microscopic kinetic equation for the particle distribution function $f(\vec{x}, \vec{v}, t)$ through moment integration.

The "Lattice" method, in which the continuous variables $\vec{x}$ and $\vec{v}$ are restricted to discrete values, is used to approximate the solution of Boltzmann's equation. The time change of these values is then described by a modified transport equation which lends it self to fast numerical solution methods.

DmQn is the most widely used abbreviation for lattice Boltzmann models where m stands for the number of dimensions (3 in our case), and n is the number of finite velocity vectors. There are different types of three dimensional discrete velocity lattice models, but not all of them have enough symmetry to ensure macroscopic isotropy [28]. By introducing a multi-speed model on a cubic lattice [19], models such as D3Q15, D3Q19 and D3Q27 are widely employed. D3Q19 is a feasible choice for our purposes, as it is more computationally stable than D3Q15 and it is more time efficient than D3Q27.

Lattice Boltzmann models also vary according to the number of fluid phases modeled and relaxation parameters governing the approach to the equilibrium. Examples include:

1. Single-phase lattice Boltzmann model with typical lattice types: D2Q9, D3Q15, D3Q19 and D3Q27 [28, 48].

2. Single and multiple relaxation models employing the assumption of an equilibrium velocity distribution and a collision operator replaced by a single-step collision towards equilibrium [4, 38, 53].

3. Multiphase lattice Bhatnagar-Gross-Krook (LBGK) models using single step relaxation and gradient terms, pseudo-potentials, or free energy functions for phase separation [31, 32, 34, 57, 58, 60].

3.1 Discretization of the Boltzmann Equation

The nonlinear collision operator of the Boltzmann equation (2.5) is simplified using the BGK (Bhatnagar—Gross—Krook) model equation (2.9), but it is not discretized. We now discuss the discretization of the Boltzmann-BGK equation

$$\frac{\partial f}{\partial t} + \vec{v} \cdot \nabla_{\vec{x}} f + \vec{F} \cdot \frac{\partial f}{\partial \vec{v}} = -\frac{f - f^e}{\tau}. \tag{3.1}$$

3.1.1 Time Discretization

Assuming no external body force ($\vec{F} = 0$), (3.1) can be formulated into an ordinary differential equation,

$$\frac{Df}{Dt} + \frac{f}{\tau} = \frac{f^e}{\tau}, \tag{3.2}$$

using the convective derivative, $\frac{D}{Dt} = \frac{\partial}{\partial t} + \vec{v} \cdot \frac{\partial}{\partial \vec{x}} = \frac{\partial}{\partial t} + \vec{v} \cdot \nabla$. Since (3.2) is a first order differential equation, its closed form solution can be formally expressed as

$$f(t + \delta t) = f(t) e^{-\frac{\delta t}{\tau}} + \frac{1}{\tau} e^{-\frac{\delta t}{\tau}} \int_0^{\delta t} e^{-\frac{s}{\tau}} g(t + s)\, ds. \tag{3.3}$$

$g(t + s) \equiv e^{\frac{2s}{\tau}} f^e(t + s)$ is a smooth function which, for δt very small, can be approximated with linear interpolation for $0 \le s \le \delta t$ by

$$g(t + s) = (1 - \frac{s}{\delta t}) g(t) + \frac{s}{\delta t} g(t + \delta t) + O(\delta t^2). \tag{3.4}$$

Using (3.4) to solve the integral term in (3.3) yields

$$\begin{aligned}
\frac{1}{\tau} e^{-\frac{\delta t}{\tau}} \int_0^{\delta t} e^{-\frac{s}{\tau}} g(t + s)\, ds &= \frac{1}{\tau} e^{-\frac{\delta t}{\tau}} \int_0^{\delta t} e^{-\frac{s}{\tau}} (1 - \frac{s}{\delta t}) g(t) + \frac{s}{\delta t} g(t + \delta t)\, ds, \\
&= \frac{1}{\tau} e^{-\frac{\delta t}{\tau}} \left[e^{\frac{s}{\delta t}} \tau g(t) - e^{\frac{s}{\tau}} \frac{(\frac{1}{\tau})^{(s-1)}}{\sqrt{\tau}} \frac{g(t)}{\delta t} + e^{\frac{s}{\tau}} \frac{(\frac{1}{\tau})^{(s-1)}}{\sqrt{\tau}} \frac{g(t + \delta t}{\delta t} \right]_0^{\delta t}, \\
&= \frac{1}{\tau} e^{-\frac{\delta t}{\tau}} g(t) \left[\tau e^{\frac{\delta}{t} \tau} - (\tau - \frac{\tau^2}{\delta t}) e^{\frac{\delta t}{\tau}} - \tau - \frac{\tau^2}{\delta t - t} \right] \\
&+ g(t + \delta t) \left[(\tau - \frac{\tau^2}{\delta t}) e^{\frac{\delta t}{\tau}} + \frac{\tau^2}{\delta t - t} \right], \\
&= g(t) - e^{-\frac{\delta t}{\tau}} g(t) + \left[1 + \frac{\tau}{\delta t} (e^{-\frac{\delta t}{\tau}} - 1) \right] \left[g(t + \delta t) - g(t) \right].
\end{aligned}$$

To first order in δt, (3.3) can be rewritten as

$$\begin{aligned} f(t+\delta t) - f(t) &= (e^{-\frac{\delta t}{\tau}} - 1)\left[f(t) - g(t)\right] \\ &+ \left(1 + \frac{\tau}{\delta t}(e^{-\frac{\delta t}{\tau}} - 1)\right)\left[g(t+\delta t) - g(t)\right]. \end{aligned} \tag{3.5}$$

Taylor expansion of $e^{-\frac{\delta t}{\tau}}$ to first order in δt gives

$$e^{-\frac{\delta t}{\tau}} \approx 1 - \frac{\delta t}{\tau}. \tag{3.6}$$

Therefore (3.5) can be simplified to

$$\begin{aligned} f(t+\delta t) - f(t) &= \left(1 - \frac{\delta t}{\tau} - 1\right)\left[f(t) - g(t)\right] \\ &+ \left(1 + \frac{\tau}{\delta t}(1 - \frac{\delta t}{\tau} - 1)\right)\left[g(t+\delta t) - g(t)\right], \\ &= -\frac{\delta t}{\tau}(f(t) - g(t)), \\ &= -\frac{\delta t}{\tau}(f(t) - f^e(t)). \end{aligned} \tag{3.7}$$

In the following sections, we describe the discretization of the velocity and the equilibrium distribution function.

3.1.2 Approximation of the Equilibrium Distribution Function

In the lattice Boltzmann equation, the equilibrium distribution function is obtained by a truncated, small macroscopic velocity ($\vec{u}$) expansion (low Mach number approximation) [27]. The Maxwell distribution (also known as the Maxwell-Boltzmann distribution) for a three dimensional system is given by

$$f^e(\rho, \vec{v}) = \frac{\rho}{(2\pi RT)^{3/2}} e^{-\frac{(\vec{v}-\vec{u})^2}{2RT}}. \tag{3.8}$$

Expanding the quadratic form in the exponent of the exponential and Taylor expansion of f^e in $\vec{u}$ up to second order gives

$$\begin{aligned} f^e &= \frac{\rho}{(2\pi RT)^{3/2}} e^{-\frac{\vec{v}^2}{2RT}} e^{\frac{\vec{v}\cdot\vec{u}}{RT}} e^{-\frac{\vec{u}^2}{2RT}}, \\ &= \frac{\rho}{(2\pi RT)^{3/2}} e^{-\frac{\vec{v}^2}{2RT}} \{f^e(0) + \vec{u}(f^e)'(0) + \frac{\vec{u}^2}{2}(f^e)''(0)\} + O(\vec{u}^3), \\ &= \frac{\rho}{(2\pi RT)^{3/2}} e^{-\frac{\vec{v}^2}{2RT}} \{1 + \vec{u}\cdot\frac{\vec{v}}{RT} + \frac{\vec{u}^2}{2}\cdot(\frac{\vec{v}^2}{(RT)^2} - \frac{1}{RT})\} + O(\vec{u}^3), \\ &= \frac{\rho}{(2\pi RT)^{3/2}} e^{-\frac{\vec{v}^2}{2RT}} \{1 + \frac{\vec{v}\cdot\vec{u}}{RT} + \frac{(\vec{v}\cdot\vec{u})^2}{2(RT)^2} - \frac{\vec{u}^2}{2RT}\} + O(\vec{u}^3). \end{aligned}$$

The local equilibrium distribution function will be used in the following form

$$f^e = \frac{\rho}{(2\pi RT)^{D/2}} e^{-\frac{\vec{v}^2}{2RT}} \times \{1 + \frac{\vec{v}\cdot\vec{u}}{RT} + \frac{(\vec{v}\cdot\vec{u})^2}{2(RT)^2} - \frac{\vec{u}^2}{2RT}\}, \tag{3.9}$$

with further discretization of the velocities as described next.

3.1.3 Discretization of Velocities

We summarize the discretization of the velocities for the D3Q27 model in this section. The velocity moments of integrals of (3.9) over the entire velocity space are needed. The moments of particle distribution functions are essential for the consistency of the Navier-Stokes equations. Isotropy, which is the most important of the Navier-Stokes symmetries, should also be retained by the discretization.

In the LBM derivation, the velocity moments are directly used as constraints for the numerical integration. For models that include temperature and for accurate results, the integration of the second moment has to be correct; since we will use an isothermal model, only the first moment of the velocity is required. The velocity moments of (3.9) in three dimensions can be written as

$$\begin{aligned} I &= \int \phi(\vec{v}) f^e \, d\vec{v}, \\ &= \frac{\rho}{(2\pi RT)^{D/2}} \int \phi(\vec{v}) e^{-\frac{\vec{v}^2}{2RT}} \{1 + \frac{\vec{v}\cdot\vec{u}}{RT} + \frac{(\vec{v}\cdot\vec{u})^2}{2(RT)^2} - \frac{\vec{u}^2}{2RT}\} \, d\vec{v}, \end{aligned} \tag{3.10}$$

where ϕ is a function containing powers of the velocity components,

$$\phi(\vec{v}) = v_1^r v_2^s v_3^t. \tag{3.11}$$

Therefore, from (3.10) and (3.11),

$$\begin{aligned} I &= \frac{\rho}{\pi\sqrt{\pi}} (\sqrt{2RT})^{-3} \int v_1^r v_2^s v_3^t e^{-\frac{\vec{v}^2}{(\sqrt{2RT})^2}} \left(1 - \frac{\vec{u}^2}{(2RT)} + \frac{2\vec{v}\cdot\vec{u}}{(2RT)} + \frac{2(\vec{v}\cdot\vec{u})^2}{(\sqrt{2RT})^4}\right) d\vec{v}, \\ &= \frac{\rho}{\pi\sqrt{\pi}} (\sqrt{2RT})^{-3} \left[\int v_1^r v_2^s v_3^t e^{-\frac{v_1^2+v_2^2+v_3^2}{(\sqrt{2RT})^2}} \, d\vec{v} \right. \\ &- \int v_1^r v_2^s v_3^t e^{-\frac{v_1^2+v_2^2+v_3^2}{(\sqrt{2RT})^2}} \left(\frac{u_1^2+u_2^2+u_3^2}{2RT}\right) d\vec{v} \\ &+ \int v_1^r v_2^s v_3^t e^{-\frac{v_1^2+v_2^2+v_3^2}{(\sqrt{2RT})^2}} \left(\frac{2(v_1u_1+v_2u_2+v_3u_3)}{2RT}\right) d\vec{v} \\ &+ \int v_1^r v_2^s v_3^t e^{-\frac{v_1^2+v_2^2+v_3^2}{(\sqrt{2RT})^2}} \left(\frac{2(v_1^2u_1^2+v_2^2u_2^2+v_3^2u_3^2)}{(\sqrt{2RT})^4}\right) d\vec{v} \\ &+ \left. \int v_1^r v_2^s v_3^t e^{-\frac{v_1^2+v_2^2+v_3^2}{(\sqrt{2RT})^2}} \left(\frac{4(v_1u_1v_2u_2+v_1u_1v_3u_3+v_2u_2v_3u_3)}{(\sqrt{2RT})^4}\right) d\vec{v} \right]. \end{aligned} \tag{3.12}$$

The integration of the first term on the RHS of (3.12) is done explicitly below, the results for the remaining three terms, which follow analogously, are merely listed.

$$
\begin{aligned}
&\frac{\rho}{\pi\sqrt{\pi}}(\sqrt{2RT})^{-3}\left(\int v_1^r v_2^s v_3^t e^{-\frac{v_1^2+v_2^2+v_3^2}{(\sqrt{2RT})^2}}\,d\vec{v}\right)\\
&= \frac{\rho}{\pi\sqrt{\pi}}(\sqrt{2RT})^{-3}\left(\int_{-\infty}^{\infty}\int_{-\infty}^{\infty}\int_{-\infty}^{\infty} e^{-\frac{v_1^2}{(\sqrt{2RT})^2}}v_1^r e^{-\frac{v_2^2}{(\sqrt{2RT})^2}}v_2^s e^{-\frac{v_3^2}{(\sqrt{2RT})^2}}v_3^t\,dv_1\,dv_2\,dv_3\right),\\
&= \frac{\rho}{\pi\sqrt{\pi}}(\sqrt{2RT})^{-3}\left(\int_{-\infty}^{\infty} e^{-\frac{v_1^2}{(\sqrt{2RT})^2}}v_1^r\,dv_1\int_{-\infty}^{\infty} e^{-\frac{v_2^2}{(\sqrt{2RT})^2}}v_2^s\,dv_2\int_{-\infty}^{\infty} e^{-\frac{v_3^2}{(\sqrt{2RT})^2}}v_3^t\,dv_3\right),\\
&= \frac{\rho}{\pi\sqrt{\pi}}\cdot\left[(\sqrt{2RT})^r\int_{-\infty}^{\infty} e^{-(\frac{v_1}{\sqrt{2RT}})^2}\left(\frac{v_1}{\sqrt{2RT}}\right)^r d\frac{v_1}{(\sqrt{2RT})}\right.\\
&\qquad\cdot(\sqrt{2RT})^s\int_{-\infty}^{\infty} e^{-(\frac{v_2}{\sqrt{2RT}})^2}\left(\frac{v_2}{\sqrt{2RT}}\right)^s d\frac{v_2}{(\sqrt{2RT})}\\
&\qquad\left.\cdot\,(\sqrt{2RT})^t\int_{-\infty}^{\infty} e^{-(\frac{v_3}{\sqrt{2RT}})^2}\left(\frac{v_3}{\sqrt{2RT}}\right)^t d\frac{v_3}{(\sqrt{2RT})}\right],\\
&= \frac{\rho}{\pi\sqrt{\pi}}(\sqrt{2RT})^{s+r+t}\cdot\left[\int_{-\infty}^{\infty} e^{-(\frac{v_1}{\sqrt{2RT}})^2}\left(\frac{v_1}{\sqrt{2RT}}\right)^s d\frac{v_1}{(\sqrt{2RT})}\right.\\
&\qquad\cdot\int_{-\infty}^{\infty} e^{-(\frac{v_2}{\sqrt{2RT}})^2}\left(\frac{v_2}{\sqrt{2RT}}\right)^r d\frac{v_2}{(\sqrt{2RT})}\\
&\qquad\left.\cdot\int_{-\infty}^{\infty} e^{-(\frac{v_3}{\sqrt{2RT}})^2}\left(\frac{v_3}{\sqrt{2RT}}\right)^t d\frac{v_3}{(\sqrt{2RT})}\right],\\
&= \frac{\rho}{\pi\sqrt{\pi}}(\sqrt{2RT})^{s+r+t}\cdot\left(\int_{-\infty}^{\infty} e^{-\varsigma_x^2}{\varsigma_x}^s\,d\varsigma_x\cdot\int_{-\infty}^{\infty} e^{-\varsigma_y^2}{\varsigma_y}^r\,d\varsigma_y\cdot\int_{-\infty}^{\infty} e^{-\varsigma_z^2}{\varsigma_z}^t\,d\varsigma_z\right),\\
&= \frac{\rho}{\pi\sqrt{\pi}}(\sqrt{2RT})^{s+r+t}I_x^s I_y^r I_z^t, \qquad (3.13)
\end{aligned}
$$

where I_i^r is the r-th moment of the function $e^{\varsigma_i^2}$.

The results for the remaining three integrals are

$$
\begin{aligned}
&-\frac{\rho}{\pi\sqrt{\pi}}(\sqrt{2RT})^{-3}\int v_1^r v_2^s v_3^t e^{-\frac{v_1^2+v_2^2+v_3^2}{(\sqrt{2RT})^2}}\left(\frac{u_1^2+u_2^2+u_3^2}{2RT}\right)d\vec{v}\\
&\qquad= -\frac{\rho}{\pi\sqrt{\pi}}(\sqrt{2RT})^{s+r+t}\left(\frac{\vec{u}}{\sqrt{2RT}}\right)^2 I_x^s I_y^r I_z^t,\\
&\frac{\rho}{\pi\sqrt{\pi}}(\sqrt{2RT})^{-3}\int v_1^r v_2^s v_3^t e^{-\frac{v_1^2+v_2^2+v_3^2}{(\sqrt{2RT})^2}}\left(\frac{2(v_1u_1+v_2u_2+v_3u_3)}{2RT}\right)d\vec{v}\\
&\qquad= \frac{\rho}{\pi\sqrt{\pi}}(\sqrt{2RT})^{r+s+t}\frac{2(u_1 I_x^{r+1}I_y^s I_z^t + u_2 I_x^r I_y^{s+1} I_z^t + u_3 I_x^r I_y^s I_z^{t+1})}{\sqrt{2RT}},
\end{aligned}
$$

$$\frac{\rho}{\pi\sqrt{\pi}}(\sqrt{2RT})^{-3}\int v_1^r v_2^s v_3^t e^{-\frac{v_1^2+v_2^2+v_3^2}{(\sqrt{2RT})^2}}\left[\frac{2(v_1^2u_1^2+v_2^2u_2^2+v_3^2u_3^2)}{(\sqrt{2RT})^4}\right.$$
$$\left.+\frac{2(v_1u_1v_2u_2+v_1u_1v_3u_3+v_2u_2v_3u_3)}{(\sqrt{2RT})^4}\right]d\vec{v}$$
$$=\frac{\rho}{\pi\sqrt{\pi}}(\sqrt{2RT})^{r+s+t}\left[\frac{u_1^2I_x^{r+2}I_y^sI_z^t+u_2^2I_x^rI_y^{s+2}I_z^t+u_3^2I_x^rI_y^sI_z^{t+2}}{RT}\right.$$
$$\left.+\frac{2(u_1u_2I_x^{r+1}I_y^{s+1}I_z^t+u_2u_3I_x^rI_y^{s+1}I_z^{t+1}+u_1u_3I_x^{r+1}I_y^sI_z^{t+1})}{RT}\right].$$

Equation (3.12) can be summarized as

$$\begin{aligned}I &= \frac{\rho}{\pi\sqrt{\pi}}(\sqrt{2RT})^{r+s+t}\left[\left(1-\frac{\vec{u}^2}{2RT}\right)I_x^rI_y^sI_z^t\right.\\&+\frac{2(u_1I_x^{r+1}I_y^sI_z^t+u_2I_x^rI_y^{s+1}I_z^t+u_3I_x^rI_y^sI_z^{t+1})}{\sqrt{2RT}}\\&+\frac{u_1^2I_x^{r+2}I_y^sI_z^t+u_2^2I_x^rI_y^{s+2}I_z^t+u_3^2I_x^rI_y^sI_z^{t+2}}{RT}\\&\left.+\frac{2(u_1u_2I_x^{r+1}I_y^{s+1}I_z^t+u_2u_3I_x^rI_y^{s+1}I_z^{t+1}+u_1u_3I_x^{r+1}I_y^sI_z^{t+1})}{RT}\right].\end{aligned}\tag{3.14}$$

Gauss-Hermite [15] quadrature can be applied to numerically integrate these moments,

$$I_x^r=\int_{-\infty}^{\infty}f(x)e^{-x^2}\,dx=\sum_{k=1}^{N}w_kf(x_k).\tag{3.15}$$

Using the Gauss-Hermite 3-point formula,

$$\varsigma_1=-\sqrt{3/2},\quad \varsigma_2=0,\quad \varsigma_3=\sqrt{3/2},\tag{3.16}$$
$$w_1=\frac{\sqrt{\pi}}{6},\quad w_2=\frac{2\sqrt{\pi}}{3},\quad w_3=\frac{\sqrt{\pi}}{6},\tag{3.17}$$

the moment function can be expressed in the following form,

$$I=\frac{\rho}{\pi\sqrt{\pi}}\sum_{i=1}^{3}\sum_{j=1}^{3}\sum_{k=1}^{3}w_iw_jw_k\phi(\varsigma_{i,j,k}),\tag{3.18}$$

where $\varsigma_{i,j,k}$ is the vector $\varsigma_{i,j,k}=(\sqrt{2RT})(\varsigma_i,\varsigma_j,\varsigma_k)^T$. As each of the three sums runs over three values, there are a total of twenty seven possible values for $\varsigma_{i,j,k}$ and $w_iw_jw_k$. For an isothermal model, the temperature T has relevance only as scaling parameter and can be replaced by a constant $c=\sqrt{3RT}$. This constant c is related to the speed

of sound by the equation $c_s \equiv \sqrt{RT} = c/\sqrt{3}$, $c_s^2 = c^2/3 = RT$ [36]. Dividing the weights by $\pi\sqrt{\pi}$, we obtain

$$\begin{aligned} w_\alpha &\equiv \frac{w_i w_j w_k}{\pi\sqrt{\pi}}, \\ &= \begin{cases} 8/27, & i=j=k=2, \quad \alpha = 0 \\ 2/27, & i=j=2, k=1, \quad \alpha = 1,\ldots,6 \\ 1/54, & i=j=1, k=2, \quad \alpha = 7,\ldots,18 \\ 1/216, & i=j=k=3, \quad \alpha = 19,\ldots,26, \end{cases} \end{aligned} \tag{3.19}$$

and

$$\vec{e}_\alpha = \begin{cases} (0,0,0)^T, & \alpha = 0 \\ (\pm 1,0,0)^T c, (0,\pm 1,0)^T c, (0,0,\pm 1)^T c, & \alpha = 1,\ldots,6 \\ (\pm 1,\pm 1,0)^T c, (\pm 1,0,\pm 1)^T c, (0,\pm 1,\pm 1)^T c, & \alpha = 7,\ldots,18 \\ (\pm 1,\pm 1,\pm 1)^T c, & \alpha = 19,\ldots,26. \end{cases} \tag{3.20}$$

With the discrete velocities, $\vec{e}_\alpha$, (3.18) becomes

$$I = \sum_{\alpha=1}^{26} W_\alpha \phi(\vec{e}_\alpha) f_\alpha^e. \tag{3.21}$$

Identifying W_α as $2\pi RT\sqrt{2\pi RT}e^{\frac{\vec{v}^2}{2RT}}$, this yields the familiar form of the equilibrium distribution function of D3Q27:

$$f_\alpha^e = w_\alpha \rho \left(1 + \frac{3(\vec{e}_\alpha \cdot \vec{u})}{c^2} + \frac{9(\vec{e}_\alpha \cdot \vec{u})^2}{2c^4} - \frac{3\vec{u}^2}{2c^2}\right). \tag{3.22}$$

The 3-point Gauss-Hermite quadrature integrates up to fifth order polynomials ($f(v_i)$ in 3.15) exactly for regular lattice models such as D2Q9 and D3Q27. Models on irregular lattices such as D3Q15 and D3Q19, can be derived using an *ansatz method* [67], as described in (§3.2) below.

3.2 The D3Q19 Lattice Model

D3Q19 is derived from a four dimensional hypercube (FDHC). The four dimensional face centered hypercube ($4D$ FCHC) lattice model limits velocities of particles to $(0,0,0,0)$,$(0,0,\pm 1,\pm 1)$, $(0,\pm 1,0,\pm 1)$,$(\pm 1,\pm 1,0,0)$, $(\pm 1,0,\pm 1,0)$,$(0,\pm 1,\pm 1,0)$, and $(0,0,\pm 1,\pm 1)$. Here there are 24 components including one corresponding to the rest particles. D3Q19 is the same as 4D FCHC without the fourth component. Projection of 4D FCHC to D3Q19 doubles the population of states in D3Q19 that have a single non-vanishing velocity component. For instance, a component corresponding to $(1,0,0)$ in the D3Q19 model is a combination of the $(1,0,0,1)$ and $(1,0,0,-1)$ components from 4D FCHC. Figure 3.1 shows the finite velocity vectors of the D3Q19 model and its two dimensional yz-plane projection (D2Q9).

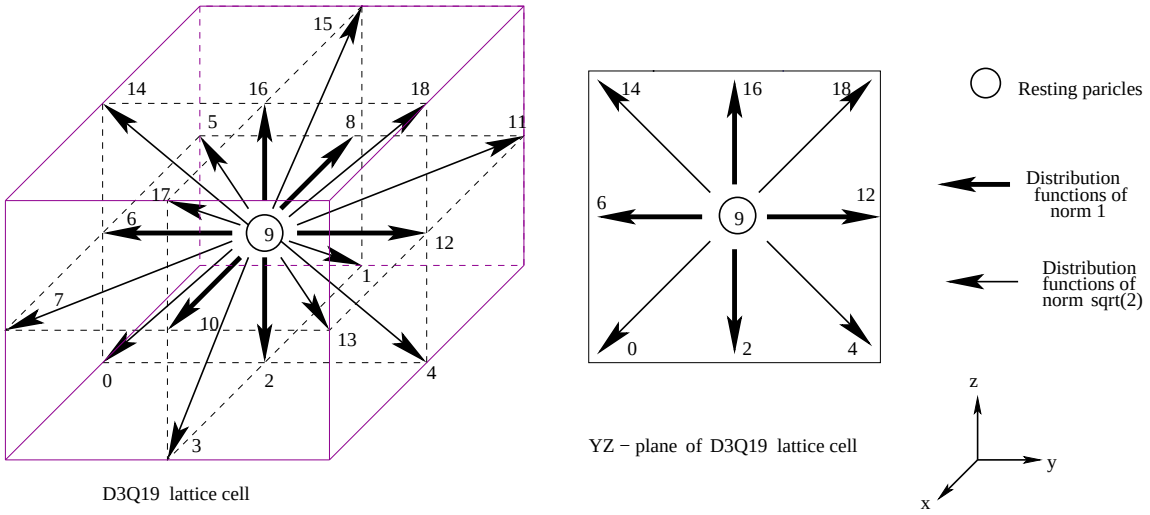

Figure 3.1: The 19 distinct velocities of the D3Q19 lattice model (left) and the 9 distinct velocities of yz-plane projection (D2Q9) (right).

The D3Q19 lattice has three sublattices (see (3.23)) and 19 discrete velocity vectors (1 "rest" velocity, 6 velocity vectors to the face centers, and 12 towards edge centers of a cube). The basic velocity vectors of the D3Q19 lattice are

$$\begin{aligned} \vec{e_\alpha} &= (\vec{e_0}, \vec{e_1}, \vec{e_2}, \vec{e_3}, \vec{e_4}, \vec{e_5}, \vec{e_6}, \vec{e_7}, \vec{e_8}, \vec{e_9}, \vec{e_{10}}, \vec{e_{11}}, \vec{e_{12}}, \vec{e_{13}}, \vec{e_{14}}, \vec{e_{15}}, \vec{e_{16}}, \vec{e_{17}}, \vec{e_{18}}), \\ &= \begin{cases} (0,0,0), & \alpha = 9, \\ (0,0,\pm 1), (0,\pm 1,0), (\pm 1,0,0), & \alpha = 2,6,8,10,12,16, \\ (0,\pm 1,\pm 1), (\pm 1,0,\pm 1), (\pm 1,\pm 1,0), & \alpha = 0,1,3,4,5,7,11,13,14,15,17,18. \end{cases} \end{aligned} \tag{3.23}$$

Weight factors for the D3Q19 model and its two dimensional yz-plane projection (D2Q9) are given in Table 3.1.

Table 3.1: Weight factors w_α for the most widely used lattice types.

Lattice model	Zero position	Simple cubic vectors (100)	Diagonal vectors(110)	cubic vectors(111)
D2Q9	4/9	1/9	1/36	do not exist
D3Q19	1/3	1/18	1/36	do not exist

3.3 The Lattice Boltzmann Method for Single Phase Flow

In a single phase lattice Boltzmann method, the distribution function of particles, $f_\alpha(\vec{x}, t)$, is an averaged quantity for the boolean lattice particle number, $n_\alpha(\vec{x}, t)$, with velocity $\vec{e_\alpha}$ at point $\vec{x}$ and t, i.e., $f_\alpha(\vec{x}, t) = \langle n_\alpha(\vec{x}, t) \rangle$. The $f_\alpha(\vec{x}, t)$ are real valued

functions with range $[0, 1]$. Mean density, momentum and velocity are given by, (here we implicitly assume the D3Q19 model),

$$\rho(\vec{x}, t) = m \sum_{\alpha=0}^{18} f_\alpha(\vec{x}, t), \tag{3.24}$$

$$\vec{p}(\vec{x}, t) = m \sum_{\alpha=0}^{18} f_\alpha(\vec{x}, t)\vec{e}_\alpha, \tag{3.25}$$

$$\vec{u}(\vec{x}, t) = \frac{\vec{p}(\vec{x}, t)}{\rho(\vec{x}, t)}. \tag{3.26}$$

The evolution of $f_\alpha(\vec{x}, t)$ is computed using the velocity discretization of (3.7),

$$f_\alpha(\vec{x} + \vec{e}_\alpha \delta t, t + \delta t) - f_\alpha(\vec{x}, t) = -\frac{\delta t}{\tau}(f_\alpha(\vec{x}, t) - f^e_\alpha(\vec{x}, t)), \qquad \alpha = 0, \ldots, 18. \tag{3.27}$$

3.4 External Body Force

Velocity and pressure boundary conditions must be imposed in an appropriate way to simulate fluid flow. Proper velocity and pressure boundaries have been proposed in [13, 30, 45]. For an incompressible fluid, an external body force and a pressure gradient have similar effects in the Navier-Stokes equations (§2.4). It is often possible to use a uniform body force [8, 22, 40, 41, 56] in lieu of pressure or velocity boundary conditions. The pressure difference at the inlet and outlet divided by the length, L of the porous media along the flow direction is the typical experimental pressure gradient i.e., $\nabla P = \frac{\Delta P}{L}$. This pressure gradient is modeled as a constant external body force and (3.27) is modified to

$$f_\alpha(\vec{x} + \mathbf{e}_\alpha \delta t, t + \delta t) - f_\alpha(\vec{x}, t) = \Omega_\alpha(\vec{x}, t) - 3\frac{w_i}{c^2}\delta t \mathbf{e}_\alpha \cdot \nabla P. \tag{3.28}$$

The body force defines the macroscopic flow direction by adding momentum to links with non-zero projection in the direction of the force and taking into account the weight factors (w_α) of the links.

3.5 Initial Conditions

Initial conditions must be chosen consistent with the physical experiment to be simulated. In our case, the initial velocity is zero ($\vec{u} = 0$) and initial density ($\rho = \rho_0$) is constant. The equilibrium distribution function (3.22) is initialized using the initial velocity and density and the $f_\alpha(\vec{x}, 0)$ are set from the equilibrium distribution function.

3.6 Boundary Conditions

Different types of boundary conditions are possible. In particular

- the no-slip boundary condition is appropriate for most fluids in contact with solid (rock) sites;
- periodic boundary conditions are useful for modeling large systems because they tend to minimize finite length effects.

3.6.1 No-slip Bounce Back Boundary Condition

In lattice Boltzmann simulations, no-slip boundary conditions are realized by the so called bounce back rule [29, 37]. When fluid particles hit a solid wall, they are reflected 180° with the same speed. Bounce back can be applied either at wall lattice sites or half way along the links between the fluid and solid lattice sites. In more complicated cases (such as curved and irregular boundaries), the no-slip boundary lies more generally between the last fluid and the first solid lattice sites, the exact placement depending on the geometry of the system, the relaxation parameter τ of the LBGK model [37, 41] and the magnitude of the forcing term [35, 65]. Fig. 3.2 depicts wall sites (three small shaded circles in the first row) where fluid particles are collided on and bounced back, and the pore sites where fluid particles are streaming through.

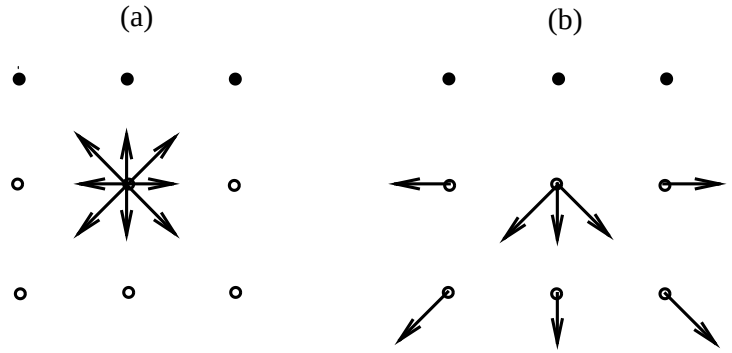

Figure 3.2: Lattice vectors at a fluid node (center point): (a) before streaming and (b) after streaming for $\delta t = 1$ time unit. The three lattice vectors at the center node in (b) result from bounce-back boundary conditions along the row of wall nodes

Several authors have proposed more sophisticated second order boundary conditions, which model a no-slip boundary exactly at the wall nodes. Many of these are restricted to regular geometries, like octagonal objects and flat walls [50, 61], but there are also general boundary-fitting models [11, 23]. However, bounce back is very attractive for simulation due to its simplicity and computational efficiency.

3.6.2 Periodic Boundary Conditions

Periodic boundary conditions are imposed in the flow (z) direction by treating pore lattice sites on the inlet and outlet faces as nearest neighbors if they have common x and y coordinates. To achieve this, the medium must (usually) be doubled in the z-direction by attaching a mirror image at one end. The new medium is now twice the length, but with geometrically matching ends. As a result, the computational volume expands by a factor of 2. Applying periodic boundary conditions preserves mass because fluid leaving the porous media at the outlet "wraps around" at the inlet,

$$f_\alpha^b(\vec{x},t)_{\text{inlet}} = f_{(18-\alpha)}^r(\vec{x},t)_{\text{outlet}}, \qquad \alpha = 0\text{–}4,14\text{–}18, \tag{3.29}$$

as shown in Figure 3.3.

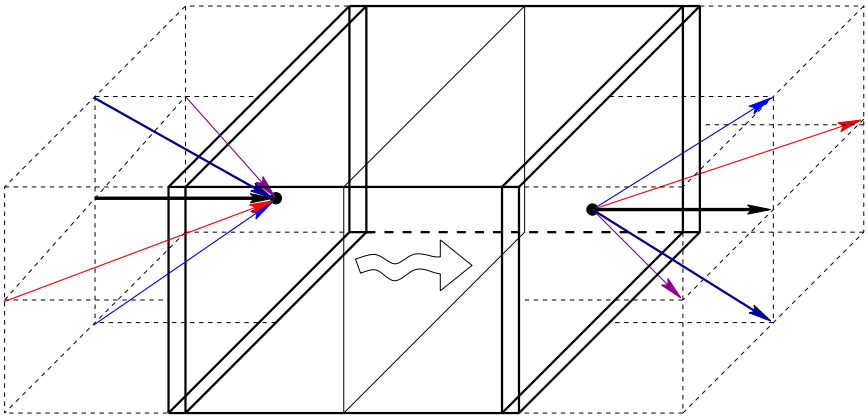

Figure 3.3: Fluid particle distribution functions leaving the outlet are reintroduced at the inlet under periodic boundary conditions. Fluid particle distribution function leaving the medium has the same color as the one entering the medium.

Chapter 4

Lattice Boltzmann Model for Two-Phase Flow in a Porous Media

Multiphase flow phenomena are characterized by movable and deformable phase boundaries at which the behavior of the flow may discontinuously change. An essential feature of immiscible two-phase flows is the occurrence of a Laplacian surface tension form of the phases which guides the system towards the reduction of interface energy [54].

4.1 From Single Phase to Two-Phase Flow

The lattice Boltzmann model in §3.3 describes the simulation of single phase flow. Here we review the extension to modeling fluid flow for two phases. We assume only red (r) and blue (b) phases whose particle distribution functions are established by the evolution of the modified lattice Boltzmann equations

$$f_\alpha^k(\vec{x} + \vec{e_\alpha}\delta t, t + \delta t) - f_\alpha^k(\vec{x}, t) = \Omega_\alpha^k(\vec{x}, t), \tag{4.1}$$

where k denotes either red or blue fluid, and

$$\Omega_\alpha^k = (\Omega_\alpha^k)_1 + (\Omega_\alpha^k)_2 \tag{4.2}$$

is the collision operator. $(\Omega_\alpha^k)_1$ represents the k^{th} single phase collision operator due to relaxation to the local equilibrium analogous to the LBGK relaxation in (2.9),

$$(\Omega_\alpha^k)_1 = -\frac{\delta t}{\tau_k}(f_\alpha^k - f_\alpha^{k(e)}), \tag{4.3}$$

and $(\Omega_\alpha^k)_2$ describes the interaction between the two phases,

$$(\Omega_\alpha^k)_2 = \vec{e_\alpha} \cdot \mathbf{F}^k, \tag{4.4}$$

where $\mathbf{F}^k$ is the sum of both fluid-fluid, $\mathbf{F}_{ff}^k$, and fluid-solid, $\mathbf{F}_{fs}^k$, interactions as explained in §4.2. Here, $f_\alpha^{k(e)}$ is the local equilibrium distribution for phase k, which

depends on the local macroscopic variables ρ^k and $\vec{u}^k$. The viscosity for phase k is determined by the value of the relaxation time τ_k for that phase (since the corresponding collision operator accounts for collisions only of the same type [54]). The equilibrium distribution can be represented in the following form for fluid particles of phase k [57],

$$f_0^{k(e)}(\vec{x},t) = \rho^k \left[d_0^k - \frac{1}{2c^2}(\vec{u}^k)^2 \right], \tag{4.5}$$

$$f_\alpha^{k(e)}(\vec{x},t) = \rho^k \left[\frac{1-d_0^k}{\phi} + \frac{D}{2\phi c^2}\vec{e_\alpha}\cdot\vec{u}^k + \frac{D(D+2)}{8\phi c^4}(\vec{e_\alpha}\cdot\vec{u}^k)^2 - \frac{D}{4\phi c^2}(\vec{u}^k)^2 \right], \quad \alpha = 0,\ldots,8,10,\ldots,18, \tag{4.6}$$

where $d_0^k (< 1)$ is a constant (the fraction of particles with zero speed equilibrium) and determines the compressibility of each component of the fluid [1]. Equations (4.5) and (4.6) are typically used for constant speed lattices such as the two dimensional hexagon ($D = 2, \phi = 6$) and the four dimensional face centered hypercube ($D = 4, \phi = 24$). Applying the projection of the 4D FCHC to obtain the D3Q19 model (as explained in §3.2), the following equilibrium equation is obtained [53],

$$f_\alpha^{k(e)}(\vec{x},t) = \begin{cases} \frac{1}{3}\rho^k \left[1 - \frac{3}{2}(\vec{u}^k)^2\right], & \text{if } \|\vec{e_\alpha}\| = 0, \\ \frac{1}{18}\rho^k \left[1 - 3\vec{e_\alpha}\cdot\vec{u}^k + \frac{9}{2}(\vec{e_\alpha}\cdot\vec{u}^k)^2 - \frac{3}{2}(\vec{u}^k)^2\right], & \text{if } \|\vec{e_\alpha}\| = 1, \\ \frac{1}{36}\rho^k \left[1 - 3\vec{e_\alpha}\cdot\vec{u}^k + \frac{9}{2}(\vec{e_\alpha}\cdot\vec{u}^k)^2 - \frac{3}{2}(\vec{u}^k)^2\right], & \text{if } \|\vec{e_\alpha}\| = \sqrt{2}. \end{cases} \tag{4.7}$$

We have taken $d_0^k = \frac{1}{3}$, $\phi = 24$, $D = 4$, and $c^2 = 1$ ($c = \frac{\delta x}{\delta t}$, $\delta x = \delta t = 1$ lattice unit). The corresponding moments of the individual phase densities and velocities, and the total density and velocity are

$$\rho^k(\vec{x},t) = m^k \sum_{\alpha=0}^{18} f_\alpha^k, \tag{4.8}$$

$$\vec{u}^k(\vec{x},t) = \frac{1}{\rho^k(\vec{x},t)} \sum_{\alpha=0}^{18} f_\alpha^k \vec{e_\alpha}, \tag{4.9}$$

$$\rho(\vec{x},t) = \sum_k \rho^k(\vec{x},t), \tag{4.10}$$

$$\vec{u}(\vec{x},t) = \frac{\sum_k (\rho^k \vec{u}^k/\tau^k)}{\sum_k (\rho^k/\tau_k)}, \tag{4.11}$$

where m^k is the mass of the constituent particles of phase k and the product $\rho(\vec{x},t)\vec{u}(\vec{x},t)$ is the total local momentum vector. The velocity field in (4.11) is a solution of the Navier-Stokes equation with kinematic viscosity ν [59],

$$\nu = \frac{1}{3}c_b(\tau_b - \frac{1}{2}) + \frac{1}{3}c_r(\tau_r - \frac{1}{2}) \tag{4.12}$$

with c_b and c_r being the fractions of red and blue phases respectively.

4.2 The Interphase Interaction Model

Modeling the flow of two immiscible fluids presents the difficulty of how to treat the dynamics at the interface between the two. These dynamics control the development of viscous fingering and dendrite formation (such as the growth of snow flakes) [7].

There are two different interaction models for the surface tension between the two phases; they must be designed to capture the phase separation of the flow. In the *chromodynamic* model [33], $(\Omega_\alpha^k)_2$ is defined in such a way that it influences the configuration of neighboring sites, enabling the pressure tensor to become anisotropic near the fluid surface. This anisotropy of the surface tension is the main source of dependence on interfacial orientation. The chromodynamic model is relatively complex from the computational perspective because of the variational minimization required by a "recoloring" step.

The other interaction model, the *pseudo-potential* approach, which remedies the deficiencies of the chromodynamic model was introduced by Shan and Chen [57]. It uses microscopic interactions to modify the surface tension related collision operator from which the interfacial force can be maintained automatically.

4.2.1 The Shan-Chen Model

To model the surface tension operator, the interaction potential $V(\vec{x}, \vec{x}')$ and the effective force on the k^{th} phase $\mathbf{F}_{ff}^k$, can be formulated as in [57],

$$V(\vec{x}, \vec{x}') = G_{kk'}(\vec{x}, \vec{x}')\phi^k(\vec{x})\phi^{k'}(\vec{x}'), \tag{4.13}$$

$$\mathbf{F}_{ff}^k(\vec{x}) = -\sum_{k'}\sum_{\alpha} V_{kk'}(\vec{x}, \vec{x} + \vec{e_\alpha})\vec{e_\alpha}, \tag{4.14}$$

where $G_{kk'}(\vec{x}, \vec{x}')$ is a Green's function. Care must be taken in the treatment of $G_{kk'}(\vec{x}, \vec{x}')$; values that insure the Galilean-invariance of the macroscopic equation in three dimensional space should be used. The transitional zone between the two fluids is controlled by $\phi^k(\vec{x})$, which is a function of the density of the k^{th} phase. The following empirical form can be used, $\phi^k = \rho_0^k[1 - exp(-\rho^k/\rho_0^k)]$, where ρ_0^k is a free parameter [12]. For simplicity, only the nearest-neighbor interactions (separation $\|\vec{e_\alpha}\|$) are involved in the Shan-Chen model. In particular,

$$G_{kk'}(\vec{x}, \vec{x} + \vec{e_\alpha}) = \begin{cases} 2G, & \text{for } \|\vec{e_\alpha}\| = 1, \\ G, & \text{for } \|\vec{e_\alpha}\| = \sqrt{2}, \\ 0, & \text{otherwise.} \end{cases} \tag{4.15}$$

$G_{kk'}$ acts likes temperature; when G, the coupling constant controlling the interaction strength, is smaller than a critical value G_c (determined by the lattice structure and initial density), the fluids separate [12].

Martys and Chen [46] have proposed an interaction force to describe the interaction between a solid and a fluid, having the form

$$\mathbf{F}_{fs}^{k}(\vec{x}) = -\rho^{k}(\vec{x}) \sum_{\alpha}^{18} W^{k} s(\vec{x} + \vec{e_{\alpha}}) \vec{e_{\alpha}}, \tag{4.16}$$

where $s = 0$ or 1 for a fluid or a solid respectively. The preference of the surface of the solid to one of the fluids (wetting) is determined by adjusting the interaction strength W^k. It is positive for a non wetting fluid and negative for a wetting fluid.

The momentum change due to the interaction forces needs to be included in the equilibrium function given by (4.7). With inclusion, the new equilibrium function becomes

$$f_{\alpha}^{k(e)}(\vec{x}, t) = \begin{cases} \frac{1}{3}\rho^{k}\left[1 - \frac{3}{2}(\vec{u}^{k(e)})^2\right], & \text{if } \|\vec{e_{\alpha}}\| = 0, \\ \frac{1}{18}\rho^{k}\left[1 - 3\vec{e_{\alpha}} \cdot \vec{u}^{k(e)} + \frac{9}{2}(\vec{e_{\alpha}} \cdot \vec{u}^{k(e)})^2 - \frac{3}{2}(\vec{u}^{k(e)})^2\right], & \text{if } \|\vec{e_{\alpha}}\| = 1, \\ \frac{1}{36}\rho^{k}\left[1 - 3\vec{e_{\alpha}} \cdot \vec{u}^{k(e)} + \frac{9}{2}(\vec{e_{\alpha}} \cdot \vec{u}^{k(e)})^2 - \frac{3}{2}(\vec{u}^{k(e)})^2\right], & \text{if } \|\vec{e_{\alpha}}\| = \sqrt{2}, \end{cases} \tag{4.17}$$

where $\vec{u}^{k(e)} = \vec{u} + \frac{\tau^k}{\rho^k}\mathbf{F}^k$ is the new velocity due to the rate of net momentum change induced at each site, $\mathbf{F}^k = \mathbf{F}_{ff}^k + \mathbf{F}_{fs}^k$. $\mathbf{F}_{ff}^k$ is the fluid-fluid interaction force given by (4.14), and $\mathbf{F}_{fs}^k$ is the fluid-solid interaction force as given in (4.16).

4.3 The Two-Phase Lattice Boltzmann Algorithm

We summarize the order of operations carried out for each "time step" in the LBM simulation. Let $\Omega \in \mathbb{R}^3$ represents a porous medium of dimensions $L_x \times L_y \times L_z$. The corresponding computational lattice is $n_x \times n_y \times n_z$ nodes with a lattice spacing $\delta x = \delta y = \delta z$. Setting the initial distribution functions, $f_\alpha(\vec{x}, 0)$, the LBM algorithm is executed for each time step in the following order:

1. compute density;
2. compute velocity;
3. compute fluid-fluid interaction;
4. compute fluid-solid interaction;
5. compute equilibrium distribution;
6. collision step;
7. streaming step;
8. apply inlet-outlet boundary condition.

(Note, as long as a consistent order is retained, the order of the steps is not important.)

4.3.1 Termination Criterion

In order to compute bulk transport properties, such as relative permeability, the velocity of each phase must reach steady state. The time step loop in the algorithm should halt when a norm in velocity change over time step δt is less than a user input tolerance, ϵ. In our calculation, steady state is assumed to be reached when the following criterion, based on the relative L_2-norm in velocity is satisfied,

$$e_b \equiv \sqrt{\frac{\sum \|\vec{u}^b(\vec{x}, t+\delta t) - \vec{u}^b(\vec{x}, t)\|^2}{\sum \|\vec{u}^b(\vec{x}, t+\delta t)\|^2}} \leq \epsilon \tag{4.18}$$

$$e_r \equiv \sqrt{\frac{\sum \|\vec{u}^r(\vec{x}, t+\delta t) - \vec{u}^r(\vec{x}, t)\|^2}{\sum \|\vec{u}^r(\vec{x}, t+\delta t)\|^2}} \leq \epsilon \tag{4.19}$$

before the number of iterations reaches the user input limit. We fixed the tolerance ϵ at 10^{-5} for our computation. If the maximum number of iterations was hit before the tolerance limits were reached, the tolerance was refined to values greater than 10^{-5}.

Chapter 5

Fontainebleau Sandstone Data Analysis

Fontainebleau sandstone is a popular reference standard due to its exceptional chemical, crystallographic and microstructural simplicity [5]. It is homogeneous, composed of grains of a single mineral (quartz) and does not contain appreciable clay [3]. As a result, a considerable amount of experimental data [25, 39] is available for Fontainebleau.

5.1 X-ray Computed Microtomographic Imaging

Synchrotron X-ray computed microtomography [14, 16, 24, 42, 63] and laser scanning confocal microscopy [26] can measure the structure of a porous material directly. The reconstructed slices can be combined into a 3D stack to reveal the geometry of the interior structure. In essence, the equipment for computed tomograph (depicted in Fig. 5.1) involves a microfocus x-ray source, a CCD (charge computed device) camera and a computer to unload the CCD array.

5.2 Segmentation

A quantitative description of the material composition in a 3D digital image using a voxel by voxel determination of phase type is known as segmentation [44]. It is used on the sandstone images to identify pore sites from rock sites. The porosity of the porous material can be directly determined from the segmented image. The Kriging-based algorithm of Oh and Lindquist [51] was used to segment our images (Fig. 5.2). In our LBM computation, there is one-to-one correspondence between a computational node and voxel, i.e., each voxel is considered as a node.

5.3 Simulation Results

Our two phase lattice Boltzmann code was run on a subvolume of size 64^3 which was extracted from a 1024^3 voxel, microtomographic image of a 22% porosity Fontainebleau sandstones. Each voxel has size 5.7 microns.

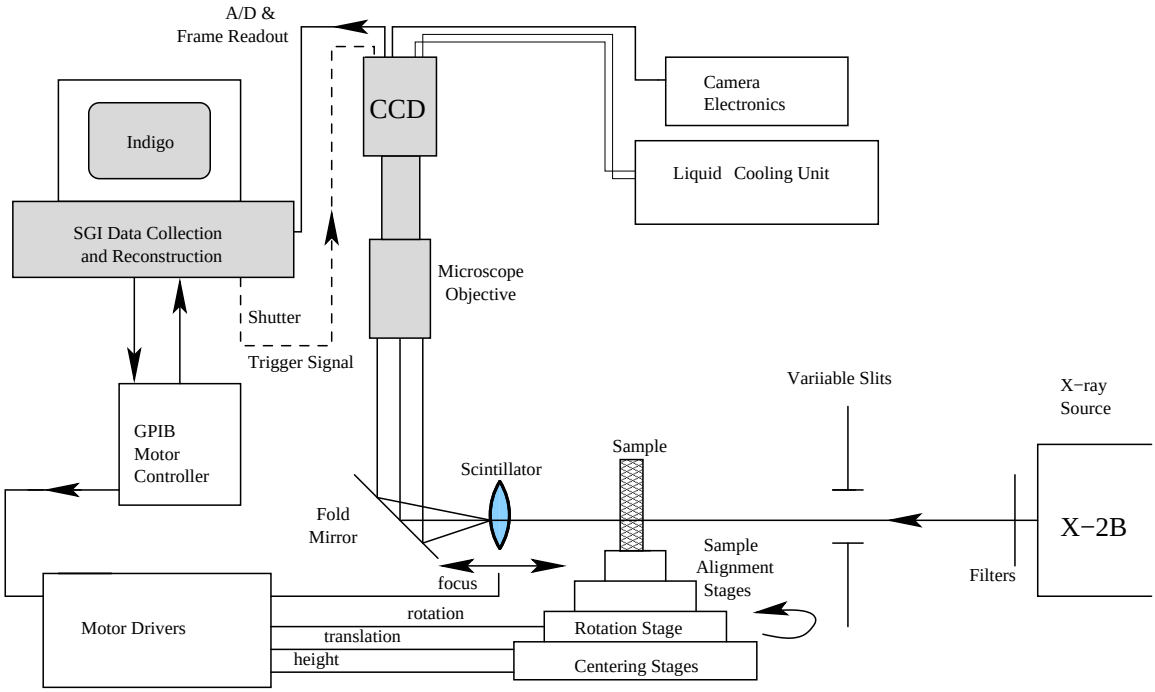

Figure 5.1: Schematic of National Synchrotron Light Source X-2B beam line CMT (computed microtomography) apparatus with array detection and expansion optics.

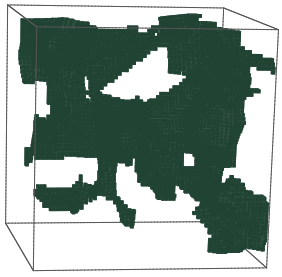

Figure 5.2: The segmented image of the pore space within a 64^3 voxel subvolume of a larger 1024^3 voxel volume of a Fontainebleau sandstone of 22% porosity. The dark shade indicates the pore space in the rock matrix, the rock phase is transparent.

Simulation results for the distribution of the two phases at different time steps are shown in the Appendix. Initially, the invading phase (blue fluid) occupied the inlet portion (the first two slices) of the Fontainebleau domain; the remaining part was filled with resident phase (red fluid) (Fig. A.1). Thereafter the blue phase displaced the red phase (Figs. A.2 to A.5) and eventually flushed the red phase from the porous medium (Fig. A.6).

The saturation of a fluid is defined as the fraction of available volume occupied

by that fluid. Thus the sum of all saturations of the fluid phases present is unity. The saturation of the resident fluid is analyzed as a function of injected fluid volume at different densities (ρ_b, ρ_r), relaxation times (τ_b,τ_r), uniform body forces (∇P) and fluid-fluid interaction constants (G) using parameter values given in Table 5.1.

Table 5.1: Parameter values used in the simulations. All measurement units are lattice based units (lu). (1 lu length = 5.7 μm, 1 lu mass = 1.85193×10^{-13} kg, and 1 lu time = 3.291×10^{-6} s).

ρ_b	1.000
ρ_r	1.000, 0.773
τ_b	0.52, 1.00, 1.50, 2.00
τ_r	0.52, 1.00, 1.50, 2.00
∇P	-0.00001, -0.00002, -0.00004, -0.00008
G	-0.001, -0.002, -0.004, -0.008

5.3.1 Relaxation Time (Viscosity Variation)

To study the effect of viscosity on the residual saturation, four different relaxation time values in the range $(0.50, 2.00]$ were chosen; outside of this range the numerical scheme becomes unstable. From (2.10),

$$\frac{\nu_b}{\nu_r} = \frac{\nu_{\text{invader}}}{\nu_{\text{resident}}} = \frac{\tau_b - \frac{1}{2}}{\tau_r - \frac{1}{2}}. \tag{5.1}$$

By keeping the relaxation time of one phase fixed at $\tau = 1$ and varying the relaxation time of the other phase through the four values of τ in Table 5.1, we can vary ν_b/ν_r over the range $[0.04, 25]$ as shown in Table 5.2.

Table 5.2: Relaxation times and their corresponding viscosity ratios.

τ_r	τ_b	ν_b/ν_r	τ_r	τ_b	ν_b/ν_r
1.00	0.52	0.04	0.52	1.00	25
	1.00	1.00	1.00		1.00
	1.50	2.00	1.50		0.50
	2.00	3.00	2.00		0.33

For these simulations the remaining parameters are set to $\nabla P = -0.00001$, $G = -0.001$, and $\rho_r = \rho_b = 1.000$. Fig. 5.3 summarizes the observed behavior of the saturation of the resident fluid with time. The results are in accord with standard observation of fluid displacement, $\nu_b/\nu_r < 1$ corresponds to stable displacement (viscosity of invading fluid greater than viscosity of resident fluid) and the resident fluid is rapidly displaced. The reverse ratio, $\nu_b/\nu_r > 1$, is unstable — the invading fluid invades via fingering. At extreme ratios, large amounts of resident fluid are by-passed.

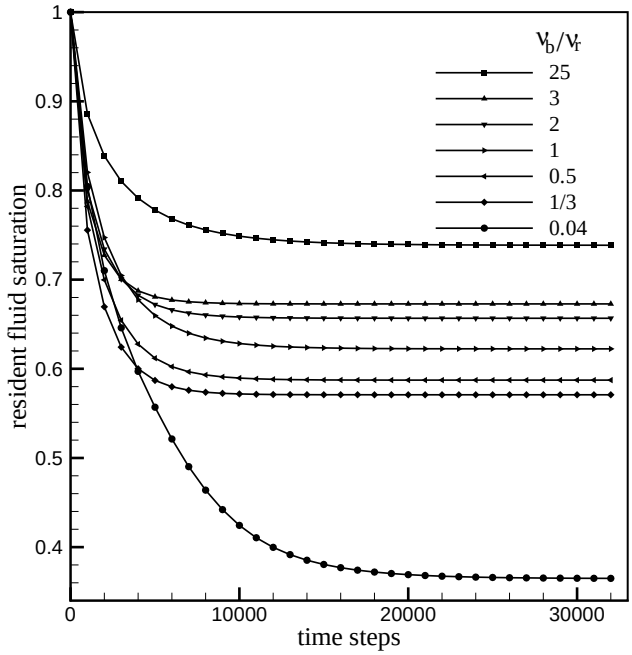

Figure 5.3: The saturation of the resident fluid versus time steps as a function of the ratio of viscosities, ν_b/ν_r.

Fig. 5.4 summarizes the residual saturation as a function of ν_b/ν_r. The rate of change of the residual saturation with respect to ν_b/ν_r is greater for $\nu_b/\nu_r < 1$ than for $\nu_b/\nu_r > 1$. The residual saturation is about 62% when $\nu_b/\nu_r = 1$. The residual saturation, S_r, is approximately related to ν_b/ν_r by $S_r(\nu_b/\nu_r) = S_r(1) + \log_{10}\left[\left(\frac{\nu_b}{\nu_r}\right)^p\right]$, where $S_r(1) = 0.680 \pm 0.004$, $p = 0.230 \pm 0.005$ for $\nu_b/\nu_r < 1$, and $S_r(1) = 0.642 \pm 0.003$, $p = 0.070 \pm 0.004$ for $\nu_b/\nu_r > 1$.

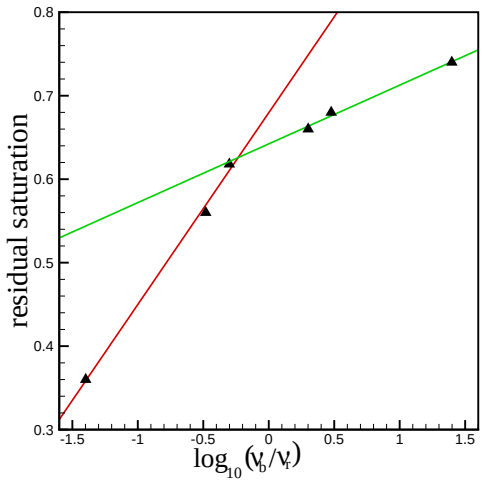

Figure 5.4: Computed residual saturation versus ratio of viscosities, ν_b/ν_r (triangles). Least squares fits to data (solid lines).

5.3.2 Body Force and Density

Results for varying the pressure gradient agree with intuition, as the pressure gradient is increased, the resident fluid saturation decreases (Fig. 5.5 (a)). Fig. 5.5 (b) summarizes the residual saturation as a function of the magnitude of the uniform body force, ∇P. The residual saturation decreases linearly with the magnitude of the body force. Their relationship can be expressed approximately by $S_r = a\,|\nabla P| + b$, where $a = (-1.70 \pm 0.03) \times 10^3$ and $b = 0.695 \pm 0.001$.

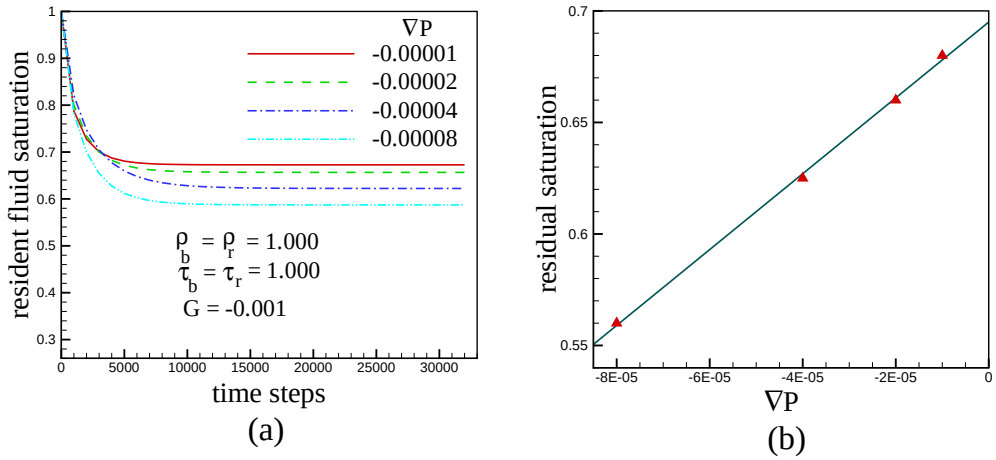

Figure 5.5: (a) The saturation of the resident fluid versus time steps as a function of different uniform body forces; and (b) computed residual saturation versus uniform body force (triangles) and least square fits to data (solid line).

The change in the initial density of the resident fluid (oil) from 1.0 to 0.773 while keeping the density of the invading fluid ρ_b to unity affects the resident saturation profile. At time step 30000 the resident fluid saturation is about 65% when its density is 1.0 and closer to 14% when its density is reduced by a factor of 0.773 (Fig. 5.6). Less dense fluids can be forced out easily than more dense ones because their dynamic viscosity, μ ($\mu = \rho\nu$, $\mu_b = \rho_b = 1.000$, $\mu_r = \rho_r = 0.773$), decreases.

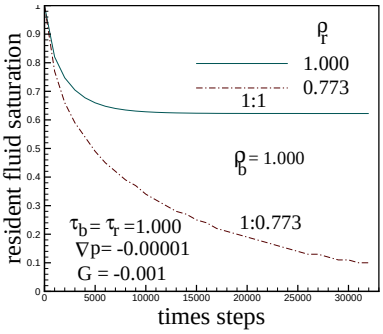

Figure 5.6: The saturation of the resident fluid versus time steps as a function of different densities.

5.3.3 Fluid-Fluid Interaction Constant

The fluid-fluid interaction term controls separation of the phases, mimicking an interfacial surface tension effect consistent with Laplace's law [46] (which states that there is a pressure drop proportional to the local curvature of the meniscus at the interface boundary between the two fluids). It is not ordinarily possible to calculate exactly a value for the critical coupling, G_c, for phase separation in three dimensional flow [47]. We therefore consider a range of values for the coupling constant G and investigate the dependence of resident fluid saturation. As the magnitude of the coupling constant increases from 0.001 to 0.008, the resident fluid saturation decreases gradually with respect to time as in Fig. 5.7 (a).

Fig. 5.7 (b) summarizes the residual saturation as a function of G. Residual saturation increases monotonically with respect to G. Hence, the phases get separated faster when the magnitude of the coupling constant is bigger.

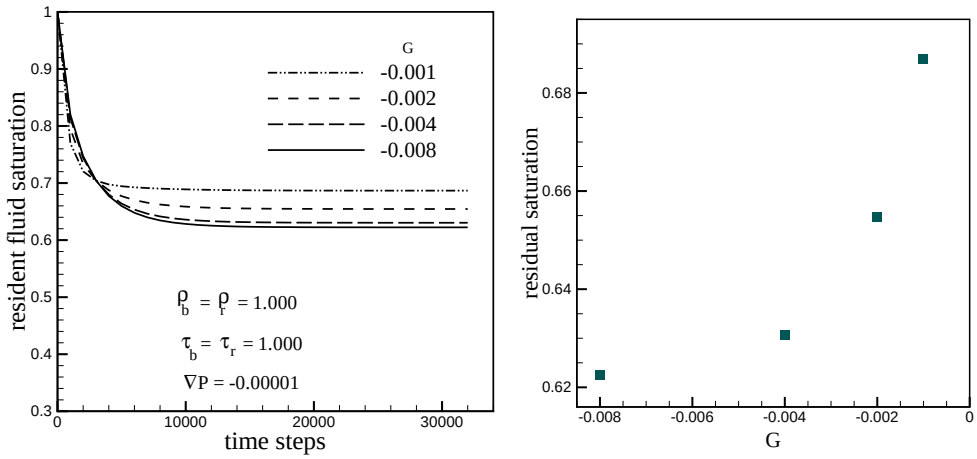

Figure 5.7: (a) The resident saturation of the red fluid (oil) versus time steps; and (b) residual saturation versus G.

5.4 Darcy's Law

Darcy's law states that the rate of saturated flow of a single fluid through a porous rock is proportional to the pressure drop per unit length along the direction of flow. The constant of proportionality is called the absolute permeability k. Specifically,

$$Q = k\frac{A}{\mu}\nabla P, \tag{5.2}$$

where Q is the volumetric flow rate, A is the cross-sectional area of the porous rock perpendicular to the flow direction (xy-plane in our case) and μ is the dynamic viscosity of the fluid. The absolute permeability k describes the ease with which fluids flow through the porous network. For a given pressure gradient, ∇P, fluid

will flow more slowly through a rock of low permeability than through one of high permeability. For the most part, the pore geometry of the rock (size and degree of connectedness of the pores) determines its permeability [7].

Consider the case in which two fluid phases ("red" and "blue") occupy the pore space of the rock. Application of a pressure gradient will cause both fluids to flow simultaneously. Darcy's law is modified to accommodate both motions,

$$Q = Q_b + Q_r, \tag{5.3}$$

$$Q_b = k_b \frac{k_0 A}{\mu_b} \nabla P, \tag{5.4}$$

$$Q_r = k_r \frac{k_0 A}{\mu_r} \nabla P, \tag{5.5}$$

where Q is the total flow rate, Q_b is the flow rate of the blue fluid, Q_r the flow rate of the red fluid, k_b and k_r are the relative permeabilities of the blue and red fluids respectively.

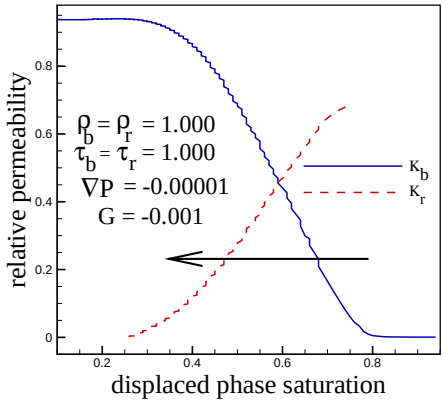

Figure 5.8: The relative permeability coefficients of the 22% porosity porous medium as a function of the displaced phase saturation. The arrow represents the direction of displaced fluid saturation during the computations.

Relative permeability depends not only on the pore geometry, which is fixed, but also on variable quantities such as the saturation of each fluid, and the spatial distribution of each phase within the pores. The sum of the two relative permeabilities is less than unity because fluid-fluid interaction increases the resistance to flow.

As shown in Fig. 5.8, as the saturation of the displaced fluid (dashed line) decreases from 1 to 0, its relative permeability, (k_r) decreases from 0.6 to 0. This is due to nonlinearities induced by fluid-fluid interfaces. For the invading fluid (solid line), the relative permeability (k_b) increases as the residual saturation of the red fluid decreases form 1 to 0. This is due to the resistance of the resident red fluid to the invading blue fluid.

Chapter 6

Conclusion

6.1 Summary

We have studied the relationship between the residual fluid saturation on controlling flow parameters, namely the driving pressure gradient (body force), the densities of the fluids and parameters of the LB model — the fluid-fluid coupling constant and the relaxation time (indirectly viscosities). The fluid saturation shows large time convergence to a residual value (Figs 5.3, 5.5 (a) and 5.7 (a)).

The residual saturation increases as the ratio of the viscosity of the invading fluid to the resident fluid, ν_b/ν_r, increases. For $\nu_b/\nu_r < 1$, the resident fluid is rapidly displaced and the displacement is stable; and for $\nu_b/\nu_r > 1$, the displacement is unstable and causes fingering (Fig 5.4).

The residual saturation decreases linearly with the magnitude of the uniform body force (∇P). A large pressure gradient forces out the resident fluid more easily than small one (Fig 5.5 (b)).

A phase with higher density decreases its saturation slower than A phase with lesser density; denser fluids can not be flushed out easily from the porous media (Fig 5.6). The residual saturation decreases monotonically as the magnitude coupling constant,G, increases (Fig 5.7 (b)).

6.2 Future Work

The performance and predictability of our work can be improved in a number of ways:

Most critical for the results of the current computation is the relatively small volume employed for these results. At 325 microns on a side (64 voxels), there are very few pores in the volume (typical sandstone grain sizes are ~ 200 – 250 microns). Thus the work here represents a proof of principal. Larger computational volumes are required in order to determine whether the residual saturation relationships implied by Figs 5.4, 5.5 (b) and 5.7 (b) are predictive. Extension to larger volumes will require parallelization of the LB code.

Fluid-solid interaction is not considered in our study. Its effect on wettability of each phase should be studied by including the fluid-solid collision operator. Furthermore, our lattice Boltzmann model is an isothermal one but in geophysical oil recovery problems temperature affects fluid flow [2]. Thermal lattice Boltzmann models such as those used by [69] can be implemented to study the effects of temperature.

We can study a wider range of viscosities using a multiple relaxation time model [18] than single relaxation time.

The error produced by no-slip bounce-back boundary condition has a linear order of convergence. Making use of curved boundary conditions which are second order accurate [49] can speed the computation.

Bibliography

[1] F. J. Alexander, H. Chen, S. Chen, and G. D. Doolen. Lattice Boltzmann model for compressible fluids. *Phys. Rev. A*, 46(4):1967—1970, 1992.

[2] L. K. Altunina and V. A. Kuvishinov. Physiochemical methods for enhancing oil recovery in oil fields. *Russ. Chem. Rev.*, 76:971–987, 2007.

[3] C. H. Arns, M. A. Knackstedt, W. Val Princzewski, and W. B. Lindquist. Accurate estimation of transport properties from microtomographic images. *Geophys. Res. Lett.*, 28(17):3361–3364, 2001.

[4] P. L. Bhatnagar, E. P. Gross, and M. Krook. A Model for Collision Process in Gases. I. Small Amplitude Processes in Charged and Neutral One-Component Systems. *Phys. Rev.*, 94:511–525, 1954.

[5] T. Bourbie and B. Zinszner. Hydraulic and acoustic properties as a function of porosity in fontainebleau sandstone. *J. Geophys. Res.*, 90:11524–11532, 1985.

[6] J. J. Brey and D. Cubero. Steady state of a fluidized granulat medium between two walls at the same temperature. *Phys. Rev. E*, 57:2019–2029, 1998.

[7] J. J. Buckles, R. D. Hazlett, S. Chen, K. G. Eggert, D. W. Grunau, and W. E. Soll. Toward Improved Prediction of Reservoir Flow Performance. *Los Alamos Science*, 22:113–121, 1994.

[8] J. Buick and C. Greated. Gravity in a lattice-Boltzmann model. *Phys. Rev. E*, 61(5):5307–5320, 2000.

[9] S. Chapman and T. G. Cowling. *The Mathematical theory of Non-Uniform Gases*. Cambridge University Press, New York, 1970.

[10] H. Chen, S. Chen, and W. H. Matthaeus. Recovery of Navier-Stokes equations using lattice-gas Boltzmann Model. *Phys. Rev. A*, 45:R5339–R5342, 1992.

[11] H. Chen, C. Teixeira, and K. Molving. Realization of Fluid Boundary Condition via Discrete Boltzmann Dynamics. *Int. J. Modern Phys. C*, 9(8):1281–1292, 1998.

[12] S. Chen and G. D. Doolen. Lattice Boltzmann method for fluid flows. *Ann. Rev. Fluid Mech.*, 30:329–364, 1998.

[13] S. Chen, D. Martinez, and R. Mei. On boundary conditions in lattice-Boltzmann methods. *Phys. Fluids*, 8(9):2527–2536, 1996.

[14] K. L. D'Amico, H. W. Deckman, J. H. Dunsmuir, B.-F. Flannery, and W. G. Roberge. X-Ray Microtomography with Monochromatic Synchrotron Radiation. *Rev. Sci. Instrum.*, 60(7):1524–1526, 1989.

[15] P. J. Davis and P. Rabinowitz. *Methods of Numerical Integration*. Academic Press, New York, 2nd edition, 1984.

[16] H. W. Deckman, J. H. Dunsmuir, K. L. D'Amico, S. R. Ferguson, and B. P. Flannery. Development of quantitative X-ray microtomography. *Matl. Res. Soc. Symp.*, 21, 1991.

[17] J. J. Derksen and H. E. A. Van den Akker. Simulation of vortex core precession in a reverse-flow cyclone. *Fluid Mechanics and Transport Phenomenon*, 6:2628–2642, 1999.

[18] D. D'Humiéres, I. Ginzburg, M. Krafczyk, P. Lallemand, and L. Luo. Muldtiple-relaxation-time lattice Boltzmann models in three dimensions. *The Royal Society*, 360:437–451, 2002.

[19] D. d'Humiéres, P. Lallemand, and U. Frisch. Lattice gas models for 3D hydrodynamics. *Europhys. Lett.*, 2:291–297, 1986.

[20] J. G. M. Eggels and J. A. Somers. Numerical Simulation of Free Convective Flow Using the Lattice-Boltzmann Scheme. *Int. J. Heat and Fluid Flow*, 16:357–364, 1995.

[21] J. G. M. Eggles. Direct and large-eddy simulation of turbulent fluid flow using the lattice-Boltzmann scheme. *Int. J. Heat and Fluid Flow*, 17:307–323, 1996.

[22] B. Ferréol and D. H. Rothman. Lattice-Boltzmann Simulations of flow through Fontainebleau Sandstone. *Transport in Porous Media*, 20(1–2):3–20, 1995.

[23] O. Filippova and D. Hänel. Boundary fitting and local grid refinement for lattice BGK models. *Int. J. Modern Phys. C*, 9(8):1271–1280, 1998.

[24] B. F. Flannery, H. W. Deckman, W. G. Roberge, and K. L. D'Amico. Three-dimensional X-ray microtomography. *Science*, 237:1439–1444, 1987.

[25] J. T. Fredrich, K. Greaves, and J. Martin. Pore geometry and transport properties of Fontainebleau sandstone. *Intl. J. Rock Mech. Min. Sci.*, 30:691–697, 1993.

[26] J. T. Friedrich, B. Menendez, and T.-F. Wong. Imaging the pore structure of geomaterials. *Science*, 268:276–279, 1995.

[27] U. Frisch, D. d'Humiéres, B. Hasslacher, P. Lallemand, Y. Pomeau, and J. P. Rivet. Lattice gas hydrodynamics in two and three dimensions. *Complex Syst.*, 1:649–707, 1987.

[28] U. Frisch, B. Hasslacher, and Y. Pomeau. Lattice Gas Automata for the Navier-Stokes Equations. *Phys. Rev. Lett.*, 56:1505–1508, 1986.

[29] M. Gallivan, D. Noble, J. Georgiadis, and R. Buckius. An evaluation of bounce back boundary condition for lattice Boltzmann simulations. *Int. J. Numer. Meth. Fluids*, 25(3):249–263, 1997.

[30] I. Ginzbourg and D.d'Humiéres. Local second-order mtheods for lattice-Boltzmann models. *J. Stat. Phys.*, 84(5–6):927–971, 1996.

[31] D. Grunau, S. Chen, and K. Eggert. Lattice Boltzmann Model for multiphase fluid flows. *Phys. Fluids A*, 5:2557–2562, 1993.

[32] A. K. Gunstensen and D. H. Rothman. Microscopic Modeling of Immiscible Fluids in the Three Dimensions by a Lattice Boltzmann Method. *Europhys. Lett.*, 18:157–161, 1992.

[33] A. K. Gunstensen and D. H. Rothman. Lattice-Boltzmann studies of immiscible two-phase flow through porous media. *J. Geophys. Research*, 98(B4):6431–6441, 1993.

[34] A. K. Gunstensen, D. H. Rothman, S. Zaleski, and G. Zanetti. Lattice Boltzmann Model of Immiscible Fluids. *Phys. Rev. A*, 43:4320–4327, 1991.

[35] Z. Guo, C. Zheng, and B. Shi. Discrete lattice effects on the forcing term in the lattice Boltzmann method. *Phys. Rev. E*, 65(4):046308, 2002.

[36] X. He and L.-S. Luo. Theory of the lattice Boltzmann method: From the Boltzmann equation to the lattice Boltzmann equation. *Phys. Rev. E*, 56:6811–6817, 1997.

[37] X. He, Q. Zou, L.-S. Luo, and M. Dembo. Some progress in the lattice Boltzmann method. Part I, non-uniform mesh grids. *J. Comp. Phys.*, 129:357–363, 1996.

[38] F. J. Higuera and J. Jiménez. Boltzmann approach to lattice gas simulations. *Europhys. Lett.*, 9:663–668, 1989.

[39] C. G. Jacquin. Corrélation entre la perméabilité et les caractéristique géométriques du grés de Fontainebleau. *Rev. Inst. Français du Pétrole*, 19:921–937, 1964.

[40] L. P. Kadanoff, G. R. McNamara, and G. Zanetti. From automata to fluid flow: Comparisons of simulation and theory. *Phys. Rev. A*, 40(8):4527–4541, 1989.

[41] D. Kandhai, A. Koponen, A. Hoekstra, M. Kataja, J. Timonen, and P. Sloot. Implementation aspects of 3D lattice-BGK: Boundaries, accuracy and a new fast relaxation method. *J. Comp. Phys.*, 150:482–501, 1999.

[42] J. H. Kinney and M. C. Nichols. X-Ray Tomographic Microscopy (XTM) Using Synchrotron Radiation. *Annu. Rev. Mater. Sci.*, 22:121–152, 1992.

[43] L. Landau and E. Lifshitz. *Fluid Mechanics*. Pergamon Press, Oxford, 1987.

[44] W. B. Lindquist, S. M. Lee, D. Coker, K. Jones, and P. Spanne. Medial axis analysis of void structure in three-dimensional tomographic images of porous media. *J. Geophys. Res.*, 101B:8297–8310, 1996.

[45] R. S. Maier, R. S. Bernard, and D. W. Grunau. Boundary conditions for the lattice Boltzmann method. *Phys. Fluids*, 8:1591–1598, 1997.

[46] N. S. Martys and H. Chen. Simulation of multicomponent fluids in complex three dimensional geometries by the lattice Boltzmann method. *Phys. Rev. E*, 53:743–750, 1996.

[47] N. S. Martys and J. F. Douglas. Critical properties and phase separation in lattice Boltzmann fluid mixtures. *Phys. Rev. E*, 63(031205):1–18, 2001.

[48] G. R. McNamara and G. Zanetti. Use of the Boltzmann Equation to Simulate Lattice-Gas Automata. *Phys. Rev. Lett.*, 61:2332–2334, 1988.

[49] R. Mei, W. Shyy, D. Yu, and L. Luo. Lattice Boltzmann method for 3-D flows with curved boundary. *J. Comput. Phys.*, 161:680–699, 2002.

[50] D. Noble, S. Chen, J. Georgiadis, and R. Buckius. A consistent hydrodynamic boundary condition for the lattice Boltzmann method. *Phys. Fluids*, 7(1):203–209, 1995.

[51] W. Oh and W. B. Lindquist. Image thresholding by indicator kriging. *IEEE Trans. Pattern Anal. Mach. Intell.*, 21:590–602, 1999.

[52] Geosciences Research Program. Complex Flow: Patterns and Predictions in the Subsurface. Technical report, 1999.

[53] Y. H. Qiana, D. d'Humiéres, and P. Allemande. Lattice BK models for Navier-Stokes equation. *Europhy. Lett.*, 17:479–484, 1992.

[54] D. Raabe. Overview of the lattice Boltzmann method for nano- and microscale fluid dynamics in materials science and engineering. *Modelling Simul. Mater. Sci. Eng.*, 12:R13–R46, 2004.

[55] J.-P. Rivet and J. P. Boon. *Lattice Gas Hydrodynamics*. Cambridge University Press, Oxford, 2001.

[56] D. H. Rothmann. Cellular automaton fluids: a model for flow in a porous media. *Geophys.*, 53:509–518, 1988.

[57] X. Shan and H. Chen. Lattice Boltzmann Model for Simulating flows with multiple phases and components. *Phys. Rev. E*, 47:1815–1819, 1993.

[58] X. Shan and H. Chen. Lattice Boltzmann Model of Simulating flows with multiple phases and components. *Phys. Rev. E*, 49:2941–2948, 1994.

[59] X. Shan and G. Doolen. Multicomponent lattice-Boltzmann method with interparticle interaction. *J. Stat. Phys.*, 81(1-2):379–393, 1995.

[60] X. Shan and G. Doolen. Diffusion in a multicomponent lattice Boltzmann equation model. *Phys. Fluids E*, 54:3614–3620, 1996.

[61] P. A. Skordos. Initial and Boundary Conditions for the Lattice Boltzmann Method. *Phys. Rev. E*, 48(6):4823–4842, 1993.

[62] J. A. Somers. Direct Simulation of Fluid Flow with Cellular Automata and the Lattice-Boltzmann Equation. *Applied Scientific Research*, 51:127–133, 1993.

[63] P. Spanne and M. L. Rivers. Computerized microtomography using synchrotron radiation from the NSLS. *Nucl. Instrum. Methods Phys. Res.*, B24/25:1063–1067, 1987.

[64] S. Succi. *The Lattice Boltzmann Equation for Fluid Dynamics and Beyond*. Clarendon Press, Oxford, 2001.

[65] R. Verberg and A. J. C. Ladd. Accuracy and stability of a lattice-Boltzmann model with subgrid scale boundary conditions. *Phys. Rev. E*, 65:016701, 2001.

[66] S. Wagner, W. Hanke, A. Bode, and F. Durst. *High Performance Computing in Science and Engineering*. Springer, Munich, 2004.

[67] Wold-Gladrow and A. Deter. *Lattice Gas Cellular Automata and Lattice Boltzmann Models*, volume 1725. Springer, Berlin/Heidelberg, 2000.

[68] Qian Y. *Lattice Gas and Lattice Kinetic Theory Applied to the Navier-Stokes Equation*. PhD thesis, University of Paris, 1990.

[69] P. Yuan and L. Shaefer. A Thermal Lattice Boltzmann Two-Phase Flow Model and Its Applications to Heat Transfer problems—Part 2. Integration and Validation. *Journal of Fluids Engineering*, 128:151–156, 2006.

[70] H. W. Zheng, C. Shu, and Y. T. Chew. Lattice Boltzmann model for multiphase flows with large density ratio. *J. Comp. Phys.*, 218:353–371, 2006.

Appendix A

The Lattice Boltzmann Simulation of Two Phases

Figs. A.1 – A.6 show the LBM simulations at selected time steps for fluid invasion into a 64^3 (Fig. 5.2) voxel subvolume of 22% porosity Fontainebleau sandstone. Values of parameters that are used in the following six simulations are: $\rho_b = 1$, $\rho_r = 1$, $\tau_b = 1$, $\tau_r = 1$, $\nabla P = -0.00001$, and $G = -0.001$.

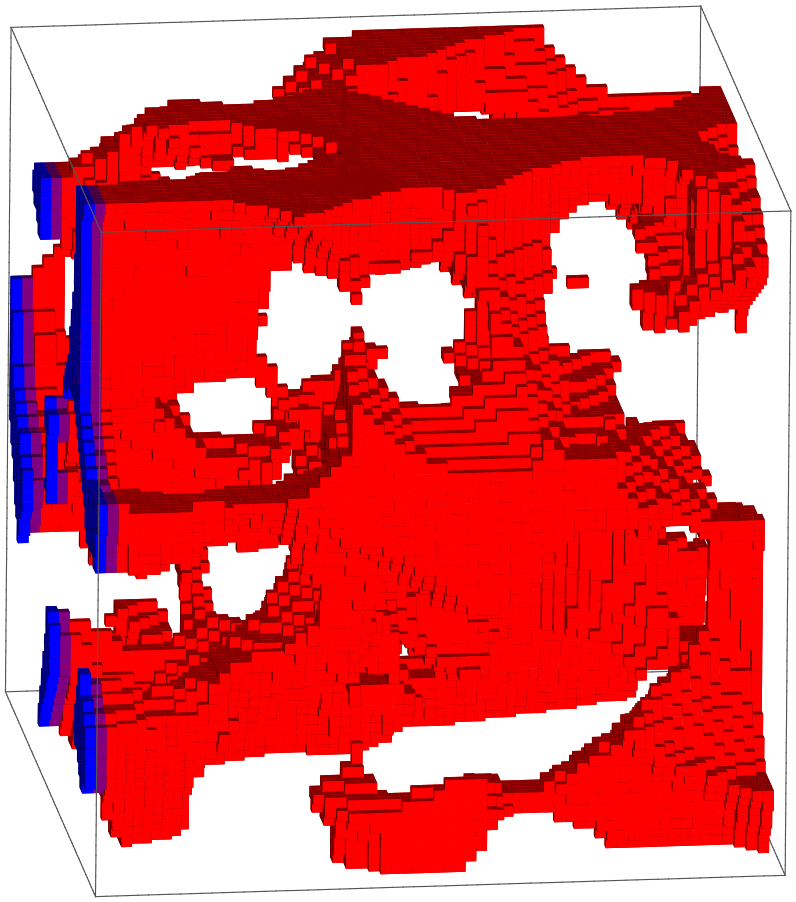

Figure A.1: Fluid distribution at time step 0

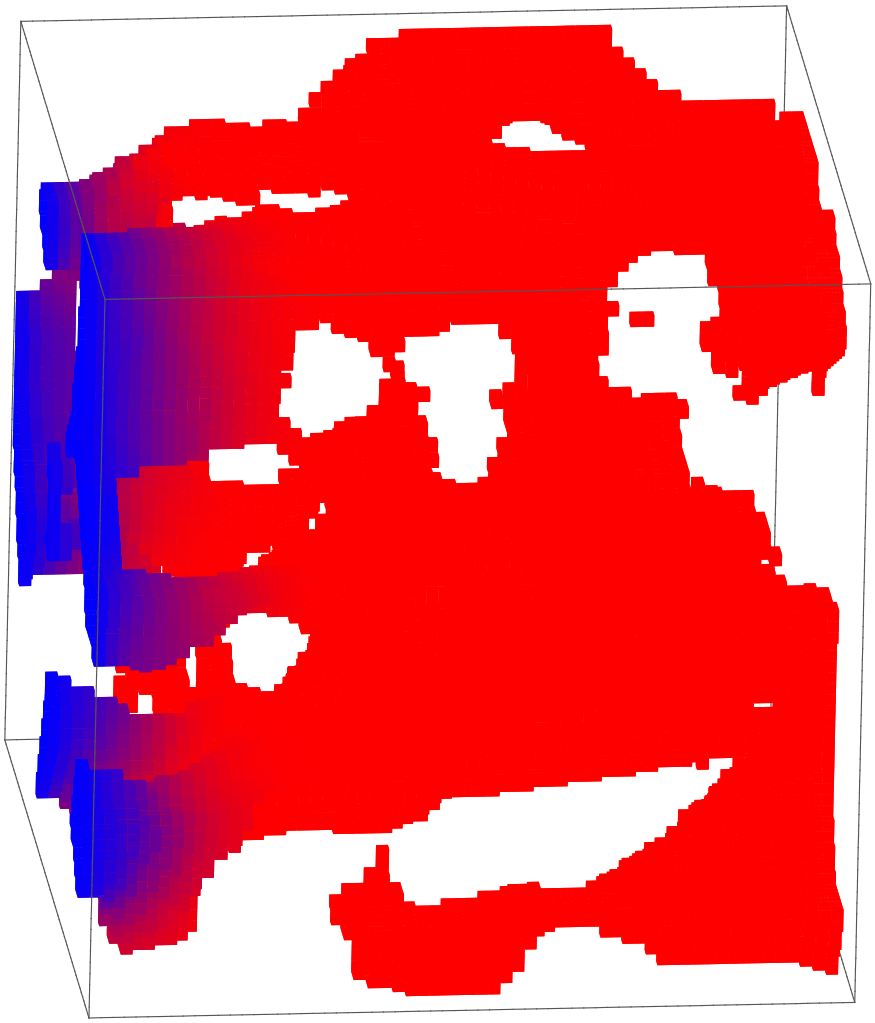

Figure A.2: Fluid distribution at time step 100

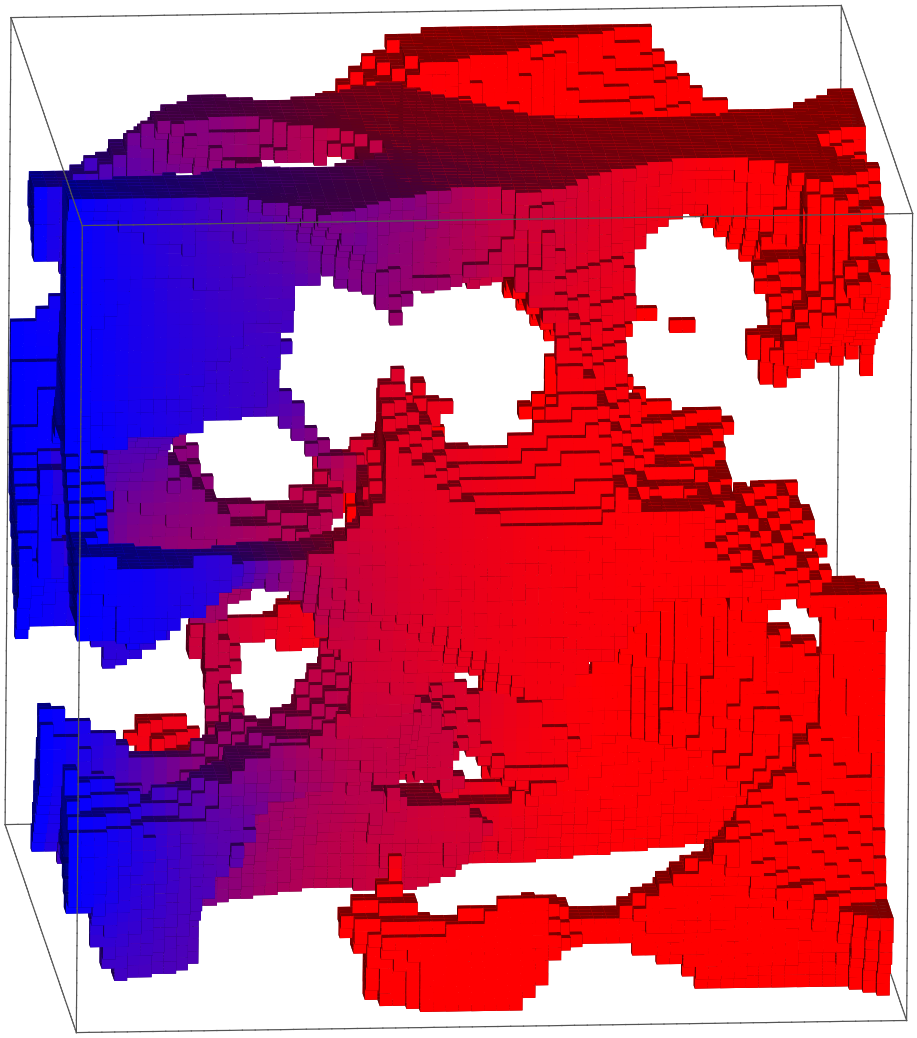

Figure A.3: Fluid distribution at time step 1000

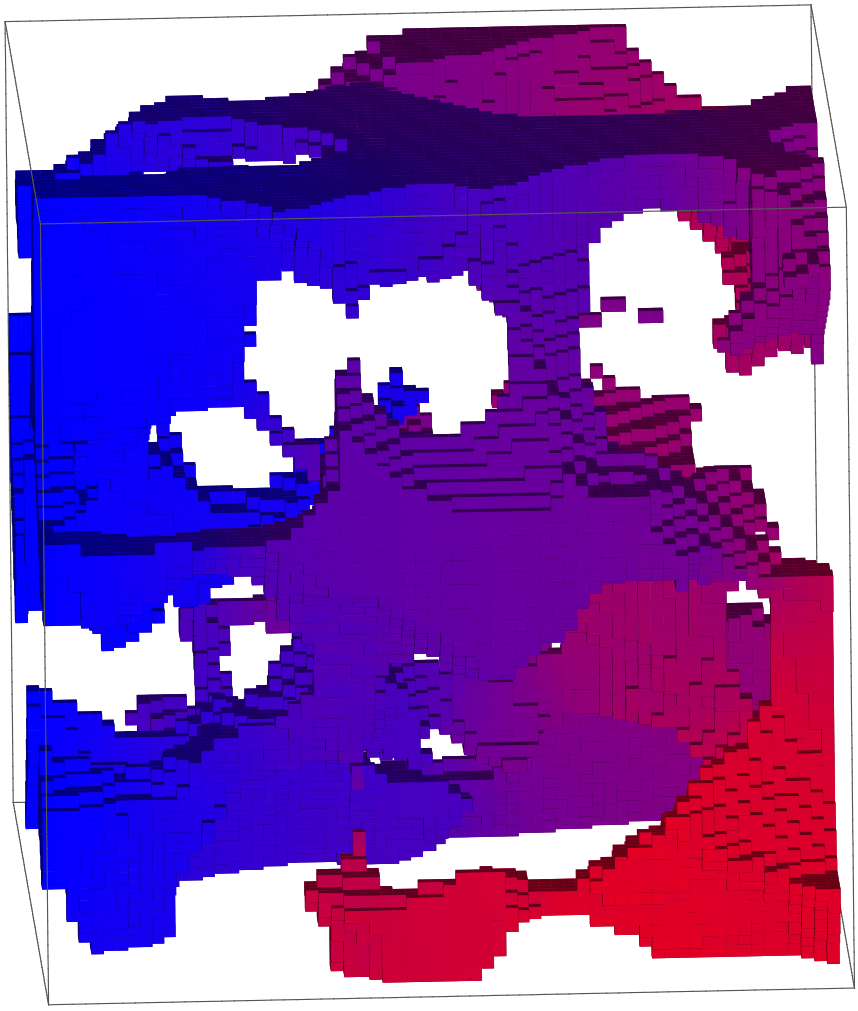

Figure A.4: Fluid distribution at time step 10000

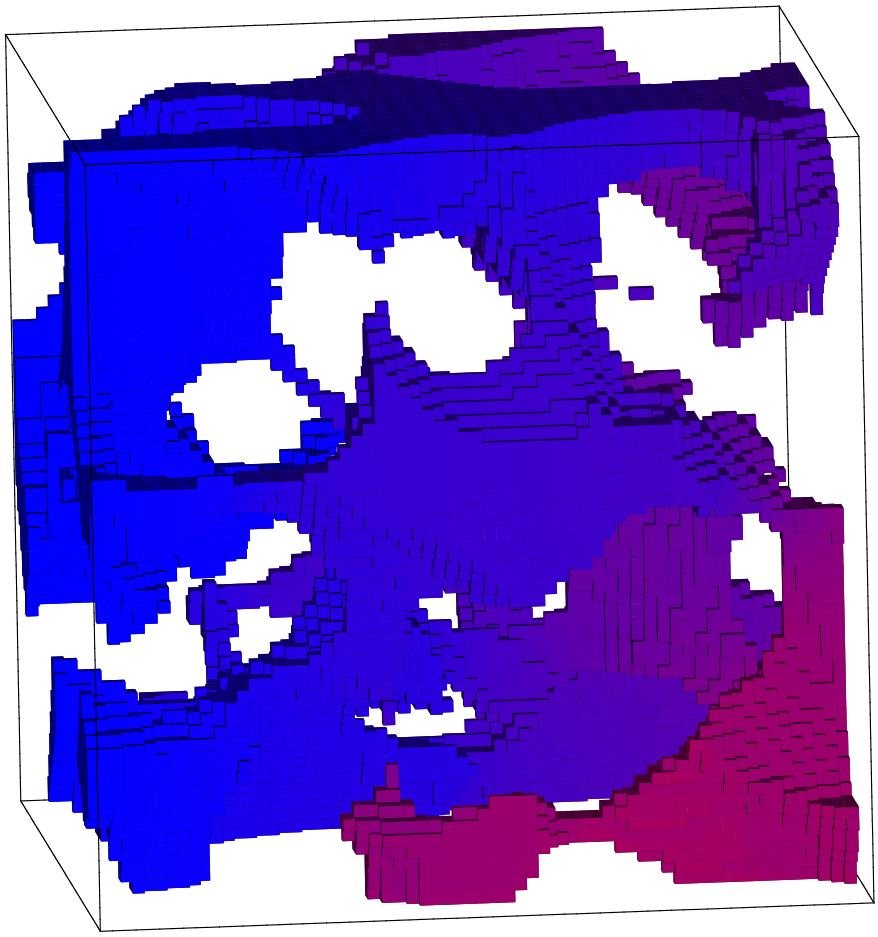

Figure A.5: Fluid distribution at time step 20000

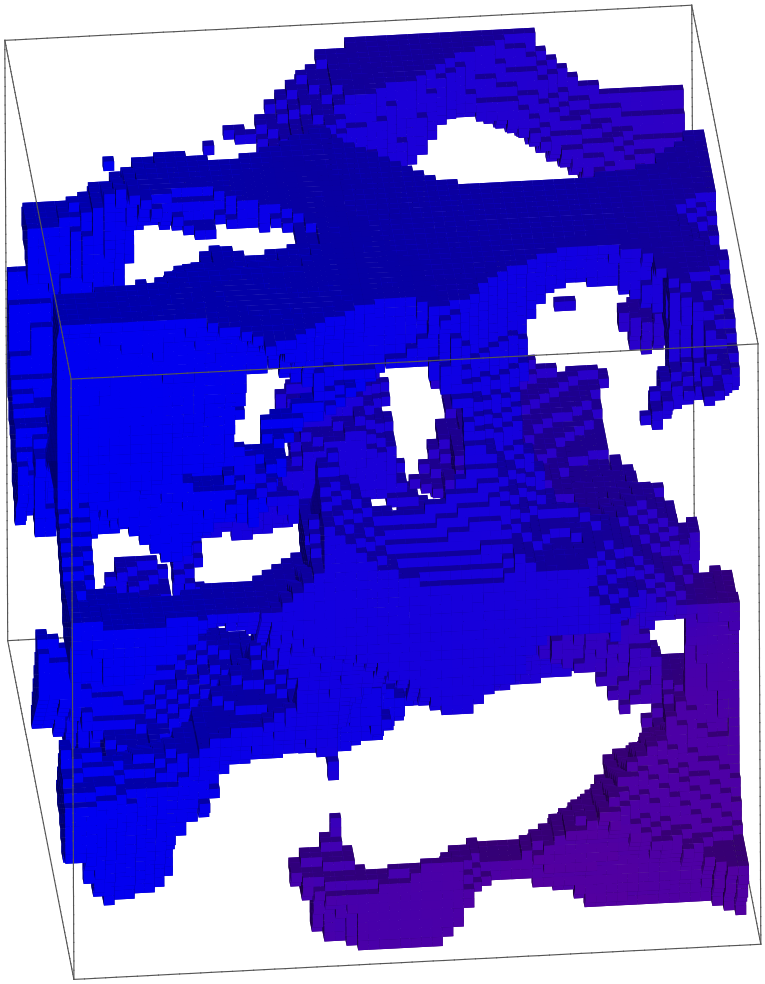

Figure A.6: Fluid distribution at time step 40000